2023 Master Thesis

Coulomb Dissociation of ^{17}B

Tokyo Institute of Technology
Department of Physics

Student ID 22M01691

Hyeji Lee

Supervisor Prof. Takashi Nakamura

Abstract

Neutron-rich isotopes have drawn much attraction in recent years due to its structural properties such as neutron halo: one or two neutrons in the nucleus are weakly bound and are spatially extended far from the core nucleus. Borromean nuclei are particularly interesting due to the two-neutron halo structure. The Borromean nucleus is a bound three-body system, where any of its two-body subsystems are unbound. Experimental data of $2n$ halo structure have been reported for ^{6}He, ^{11}Li, and ^{19}B. These $2n$ halo nuclei show a dineutron correlation, a spatially compact neutron pair, and the recent Coulomb dissociation of ^{19}B revealed the dineutron in ^{19}B. My thesis work focuses on ^{17}B, which is also considered as a $2n$ halo nucleus. ^{17}B is the core of the $2n$ halo nucleus ^{19}B but ^{17}B itself is the $2n$ halo nucleus. Investigating a dineutron correlation in ^{17}B will give us a critical information about multi-neutron halo structure in neutron-rich isotopes.

To investigate two neutron halo structure of ^{17}B, the Coulomb dissociation experiment was performed at SAMURAI (Superconducting Analyzer for MUlti particles from RAdio Isotope beams) spectrometer at RIBF (Radioactive Isotope Beam Factory), RIKEN. A ^{48}Ca primary beam accelerated to 345 MeV per nucleon was incident on a primary Be target to produce a ^{17}B secondary beam. The generated secondary beam was separated and identified by BigRIPS fragment separator and was incident on a secondary Pb target where ^{17}B is dissociated into ^{15}B and two neutrons. The charged fragment ^{15}B was detected by the SAMURAI spectrometer, while the two neutrons were detected by the neutron detector array NEBULA to measure Coulomb dissociation exclusive cross sections. We successfully extracted the two-neutron removal cross sections 617$\pm$21 (*stat.*) mb for lead target and 159$\pm$3 (*stat.*) mb for carbon target and constructed the relative energy spectrum between ^{15}B and two neutrons using the invariant mass method. This result yielded a spectrum of the reduced transition probability for electric dipole, $B(E1)$ distribution, with the photon equivalent method and Coulomb Dissociation cross sections spectrum. The obtained $B(E1)$ spectrum has wider width and smaller strength compared to that of ^{19}B and the integrated $B(E1)$ value up to 7 MeV was 1.32 $\pm$ 0.06 e^{2}fm^2 which also smaller than the one of ^{19}B in a range up to 6 MeV,

indicating the hindered halo structure of ^{17}B. The dineutron correlation in ^{17}B was also discussed.

Contents

List of Figures

List of Tables

Chapter 1

Introduction

1.1 Overview of Neutron Halo Nuclei

Over recent years, the study of neutron-rich nuclei has provided invaluable insights beyond the conventional nuclear models. A particularly intriguing subclass of neutron-rich nuclei is the *neutron halo nuclei* [3][4], characterized by an extended halo of one or two loosely bound neutrons far from the core nucleus. The first discovery of a neutron halo nucleus was ^{11}Li by I. Tanihata et al. [1]. As shown in Figure 1.1, ^{11}Li has a huge radius compared to the neighboring He, Li, Be and C isotopes with similar atomic mass numbers. Based on this discovery, I. Tanihata et al. proposed that ^{11}Li has either a large deformation or a long tail in its matter distribution. Subsequently, P. G. Hansen and B. Jonson [5] identified ^{11}Li as a neutron halo nucleus, based on its large neutron radius relative to its ^{9}Li core.

Further research on neutron halo nuclei has led to additional criteria for identifying them. One notable criterion is a small neutron separation energy. Compared to the separation energy of stable nuclei, typically around S_n = 6 to 8 MeV, neutron halo nuclei have extremely small separation energies, less than 1 MeV. This leads to a large nuclear radius. This relationship between neutron separation energy and large radius can be understood from a simple example: Assume a core of nucleons which we model with a square-well potential given by

$$V(r) = \begin{cases} -V_0 & (r \leq R) \\ 0 & (r > R) \end{cases} \tag{1.1}$$

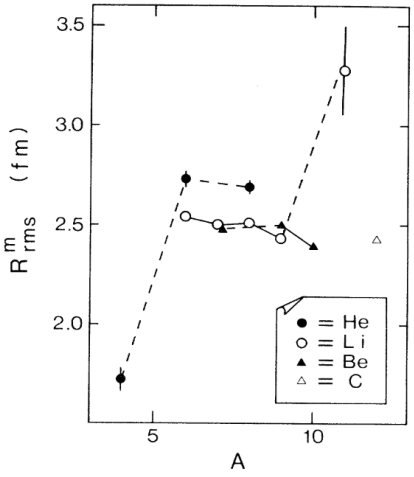

Figure 1.1: Matter RMS radius of He, Li, Be and C isotopes. ^{11}Li has a significantly larger radius than its neighbors He, Li, Be, and C [1].

A single neutron in the system will have a wavefunction outside of the potential given by

$$\Psi(r) = \left(\frac{2\pi}{k}\right)\left(\frac{e^{-kr}}{r}\right)\left[\frac{e^{kR}}{(1+kR)^{1/2}}\right], \tag{1.2}$$

where for simplification we consider only $l = 0$. And the factor k is given by

$$k = \sqrt{2\mu E/\hbar^2}, \tag{1.3}$$

where μ is the effective mass of the system and E is an eigenvalue of this wavefunction. In that case the neutron density distribution is given by

$$\rho(r) = |\Psi(r)|^2 \propto \frac{e^{-2kr}}{r^2}, \tag{1.4}$$

where the factor k determines the tail of the distribution. When k is small the distribution will have a long tail and vice versa. A long tail means that the nucleus has a large radius. We can then set $E = S_n$ to see that a small neutron separation energy gives a long tail and hence a large radius.

The narrow momentum distribution is also the criterion of halo nuclei. The momentum distri-

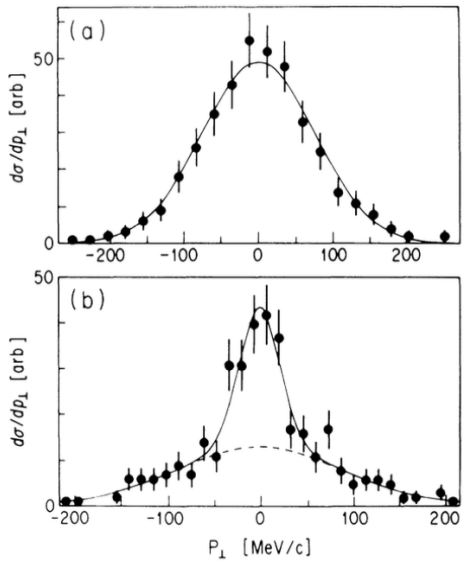

Figure 1.2: The momentum distribution of (a) ^{6}H resulting from the ^{8}H + C reaction, and (b) ^{9}Li from ^{11}Li + C reaction. Notably ^{9}Li has extremely narrow momentum distribution, characterized by a narrow Gaussian peak with $\sigma = 23 \pm 5$ MeV/c. [6]

bution of a neutron [$f(p)$] can be described by the Fourier transform of the eq. (1.2),

$$f(p) = \frac{C}{p^2 + (\hbar k)^2}, \tag{1.5}$$

where p represents the momentum of the neutron and the width of the distribution is defined by k which is related with the separation energy. This illustrates the Heisenberg's uncertainty principle: The smaller k, the wider density distribution, and the narrower momentum distribution. In Figure 1.2, the momentum distribution of ^{6}H and ^{9}Li are presented. ^{6}H has a broad momentum distribution, with $\sigma = 77 \pm 5$ MeV/c, attributed to the non-halo structure of ^{8}H. Conversely, ^{9}Li has a significantly narrower momentum distribution, with a Gaussian peak at $\sigma = 23 \pm 5$ MeV/c, which indicates ^{11}Li is a halo nucleus.

Another critical criterion of halo nuclei is the orbital angular momentum of the valence neutron. The shape of the momentum distribution is influenced not only by the separation energy but also by the orbital angular momentum (l) due to the effect of the centrifugal barrier. The width of centrifugal barrier is proportional to $l(l+1)/r^2$, significantly affecting the neutron's density distribution. Riisager et al. [7] have performed calculations on the radius of a one-neutron halo

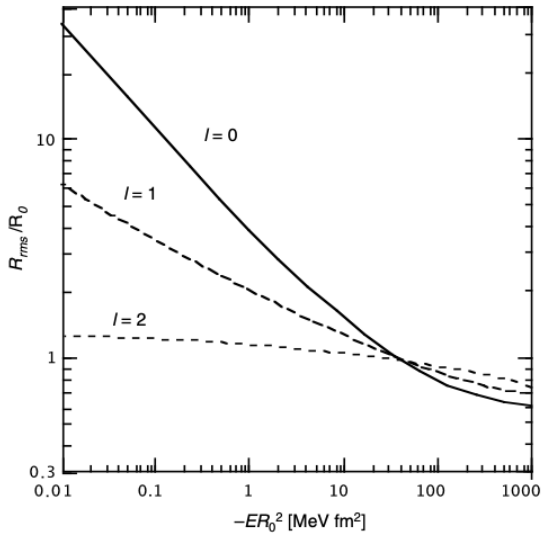

Figure 1.3: The rms radius of one-neutron halo for various separation energies and orbital angular momenta. [7]

system within a square-well potential, considering various separation energies and orbital angular momenta. In Figure 1.3, the x-axis represents the separation energy normalized by the size of the well potential R_0, while the y-axis signifies the root-mean-square (rms) radius, also normalized by R_0. It is observed that the rms radius for l = 0 or l = 1 tends to increase significantly as the separation energy nears zero, suggestive of halo formation. However, for l = 2, the rms radius remains close to R_0, indicating that it is challenging for nuclei with l = 2 or higher to develop a halo structure. Through the consideration of halo nuclei criterion so far, we can understand the development mechanism of halo structures. A halo structure tends to be developed under conditions of low neutron separation energy, typically less than 1 MeV, and a low orbital angular momentum of l = 0 or 1. With these conditions, the density distribution of the valence neutron(s) can extended to the outside of the core, leading to the formation of a halo structure.

Of all the criteria of halo nuclei, this work has a particular focus on the soft electric dipole ($E1$) mode, commonly referred to as soft $E1$ excitation. This phenomenon was predicted by P. G. Hansen and B. Jonson [5], as well as K. Ikeda et al.[8]. Halo nuclei, comprised by a core and loosely bound valence neutron(s), can be polarized by an external electric field making the valence neutron(s) oscillate against the core nucleus. The soft $E1$ excitation mode between core and valence neutron(s) has a very low energy, typically less than 1 MeV, as the halo structure easily responds

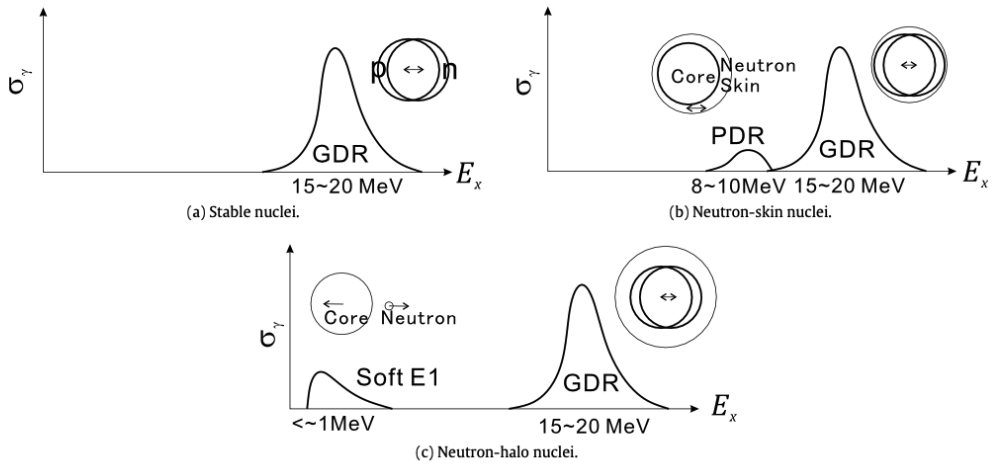

Figure 1.4: The schematic representation of $E1$ response of (a) stable nuclei, (b) neutron-skin nuclei and (c) neutron halo nuclei. [9]

to the external electric field. Figure 1.4 illustrates the $E1$ response of stable nuclei, neutron-skin nuclei and neutron halo nuclei. The $E1$ response appears in the photon absorption cross section σ_γ and the cross section is related to the reduced transition probability $B(E1)$ by eq. (2.2). The giant dipole resonance (GDR) a high-energy dipole excitation mode around 15 - 20 MeV, arises from the oscillation between proton and neutron fluids. In neutron-skin nuclei, the pigmy dipole resonance (PDR) appears in mid-energy region ($\sim$ 10 MeV) due to the vibration between the neutron skin and core. The soft $E1$ excitation occurs in very low energy region, below 1 MeV, by the vibration between the core and loosely bounded valence neutron.

The strength of the dipole excitation mode can be quantified by the $E1$ reduced transition probability $B(E1)$. The term 'reduced' in the context implies that the transition matrix element is independent of the magnetic sub-state of the initial and final states, according to the Wigner-Eckart theorem. The $E1$ reduced transition probability is defined as,

$$B(E1) = \sum_{m_i, m_f} |\langle \Phi_f | e_{eff}^{E1} \hat{T}(E1) | \Phi_i \rangle|^2 \tag{1.6}$$

$$= \frac{1}{2J_i + 1} |\langle \Phi_f || e_{eff}^{E1} \hat{T}(E1) || \Phi_i \rangle|^2, \tag{1.7}$$

where J_i is the nuclear spin of the initial state, e_{eff}^{E1} is effective charge, $\hat{T}(E1)$ represents the $E1$ transition operator, and Φ_i and Φ_f are the initial and final states of the system respectively. Assum-

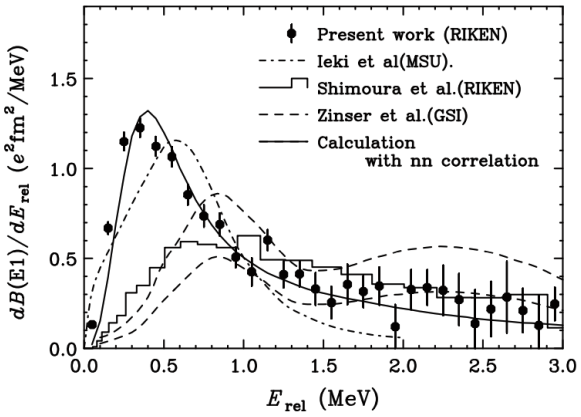

Figure 1.5: B(E1) distribution of ^{11}Li [10]

ing the direct decay from halo nuclei by photon absorption, the $E1$ reduced transition probability for relative energy between core and halo neutron E_{rel} can be rewritten as,

$$\frac{dB(E1)}{dE_x} = |\langle \Phi^f(\vec{r},\vec{q})||e^{\mathrm{E1}}_{eff}\hat{T}(E1)||\Phi^i(\vec{r})\rangle|^2 \tag{1.8}$$

$$= |\langle \exp(i\vec{r}\cdot\vec{q})||e^{\mathrm{E1}}_{eff} r Y_1(\Omega)||\Phi^i_{g.s.}\rangle|^2, \tag{1.9}$$

which have the relative position vector between center of core and halo neutron $\vec{r}$ and the relative momentum $\vec{p} = \sqrt{2\mu E_{rel}}/\hbar$ as their component. To simplify, we assume the final state Φ_f as a plane wave as,

$$\Phi_f(\vec{r},\vec{q}) = \exp(i\vec{r}\cdot\vec{q}). \tag{1.10}$$

Then the $dB(E1)/dE_{rel}$ become a form of Fourier transform of the wavefunction of ground state $\Phi_{g.s}(\vec{r})$ which multiplied by $\vec{r}$ and $E1$ transition operator. It means that when the relative momentum q is small, the strength of $B(E1)$ is large. A small q related to small $E_{rel} = E_x - S_n$ and this is the reason why the soft $E1$ excitation is observed in low excited energy region. The figure 1.5 shows the $B(E1)$ distribution of ^{11}Li. The peak of the $B(E1)$ distribution is observed around 0.3 MeV, which is the soft $E1$ excitation mode.

In the two neutron halo case, the dineutron correlation is predicted by A. B. Migdal [17]. When we assume the orbital mixture of valance neutrons in ^{11}Li, we can write the ^{11}Li wavefunction as

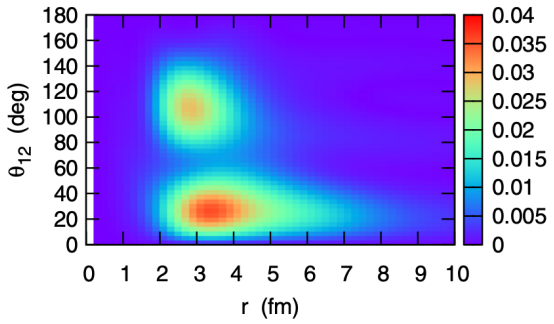

Figure 1.6: The opening angle distribution in ^{11}Li. [15]

follows:

$$\Psi(^{11}\mathrm{Li}) = \psi(^{9}\mathrm{Li}) \otimes [\alpha|1p_{1/2}\rangle^2 + \beta|2s_{1/2}\rangle^2] \tag{1.11}$$

And the expectation value of the angle between two valance neutrons $\langle\cos\theta_{nn}\rangle$ can be calculated as follows:

$$\begin{aligned}\langle\cos\theta_{nn}\rangle &= \langle\Psi(^{11}\mathrm{Li})|\cos\theta_{nn}|\Psi(^{11}\mathrm{Li})\rangle \\ &= \alpha^2\langle(1d_{5/2})^2|\cos\theta_{nn}|(1d_{5/2})^2\rangle + \beta^2\langle(2s_{1/2})^2|\cos\theta_{nn}|(2s_{1/2})^2\rangle \\ &\quad + 2\alpha\beta\langle(1d_{5/2})^2|\cos\theta_{nn}|(2s_{1/2})^2\rangle \\ &= 2\alpha\beta\langle(1d_{5/2})^2|\cos\theta_{nn}|(2s_{1/2})^2\rangle \end{aligned} \tag{1.12}$$

From here, we can see that the $\langle\cos\theta_{nn}\rangle$ is only related with the orbital mixing term, which means the orbital mixing makes the dineutron correlation. The dineutron correlation is calculated in ^{11}Li case. (Figure 1.6) The result shows that the dineutron correlation is strongly developed in ^{11}Li, where the opening angle of two neutron $\theta_{12} \sim 20^\circ$.

1.2 The Halo Structure of ^{17}B

There are two two-neutron halo nuclei in boron isotopes, ^{17}B and ^{19}B. Both nuclei have been considered as a two neutron halo nuclei because of the small two neutron separation energy and large radius[20]. Both nuclei have the valance neutrons occupied in sd-shell, which makes the orbital mixing of $1d_{5/2}$ and $2s_{1/2}$ of valance neutrons. If the two valance neutrons occupy the

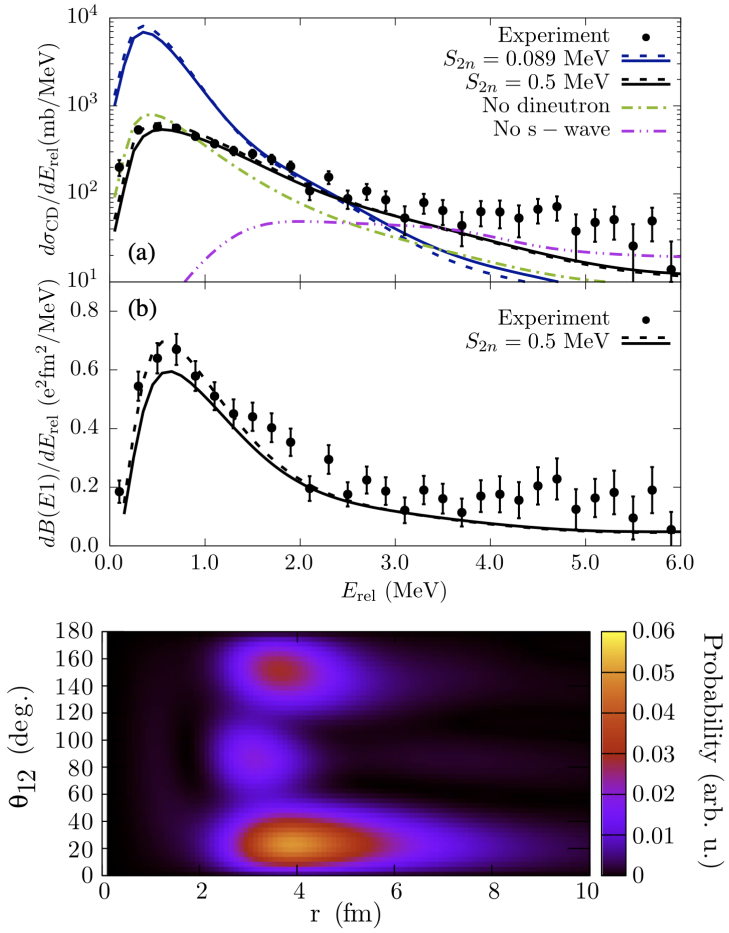

Figure 1.7: (Top)The $B(E1)$ distribution of ^{19}B. The peak at 0.5 MeV means the soft $E1$ excitation of ^{19}B[23]. (Bottom) The opening angle distribution of two valance neutrons of ^{19}B[15].

$2s_{1/2}$ orbital, the halo structure can be developed. On the other hand, if the valance neutrons occupy mainly the $1d_{5/2}$ orbital, the halo structure cannot be developed.

Recently, in boron isotopes, the reduced $E1$ transition probability of ^{19}B is observed by K. J. Cook et al.[23] using Coulomb dissociation method. The result of K. J. Cook et al. extracted the reduced $E1$ transition probability of ^{19}B and the peak was observed around 0.5 MeV. This result shows that the ^{19}B has very strong soft $E1$ mode, which means that the halo structure of ^{19}B is developed. Also, a dineutron correlation is calculated in ^{19}B case [15], and the result shows that the dineutron correlation is strongly developed in ^{19}B. In figure 1.7, the $B(E1)$ distribution of ^{19}B and the opening angle of two neutron of ^{19}B are shown.

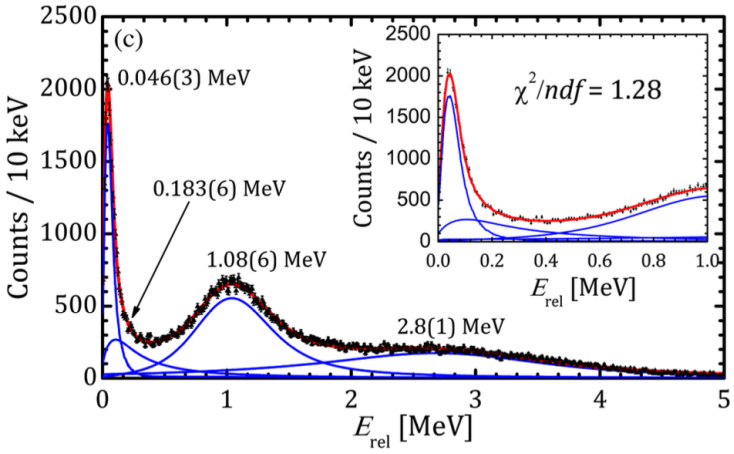

Figure 1.8: The relative energy distribution of ^{16}B.[24]

After revealing the structure of ^{19}B, the structure of ^{17}B got attention. After T. Suzuki[20], the spectroscopic factor between two orbital in sd-shell of ^{17}B has been obtained which indicates a large percentage of s-orbital as 36(19)%, 69(20)%, 50(10)% [20] [21] [22]. But recently, Z. H. Yang et al. [24] suggested a strong evidence that ^{17}B might not be a two-neutron halo nuclei. He performed the quasi-free (p, pn) scattering reaction and extracted the relative energy distribution of ^{16}B. He assumed that the knocked-out neutron from the ^{17}B should almost come from $1d_{5/2}$ or $2s_{1/2}$ orbital and got the relative energy distribution of ^{16}B. (Figure 1.8) And also, he obtained the spectroscopic factors for $1d_{5/2}$ and $2s_{1/2}$ orbital and there was surprisingly small percentage 9(2)% of $2s_{1/2}$ orbital which is very different from the past researches. Also A. Estradé et al. [25] shows proton radii of boron isotope. In this research, ^{17}B has very thick neuron surface, 0.51(11) fm, which might indicates a neutron skin structure.

So, in this research, we study the Soft E1 excitation of ^{17}B for the first, which can be the final key for deciding halo strength of ^{17}B. In this thesis, we will discuss the Coulomb Dissociation of ^{17}B as a tool for searching the Soft E1 excitation of ^{17}B.

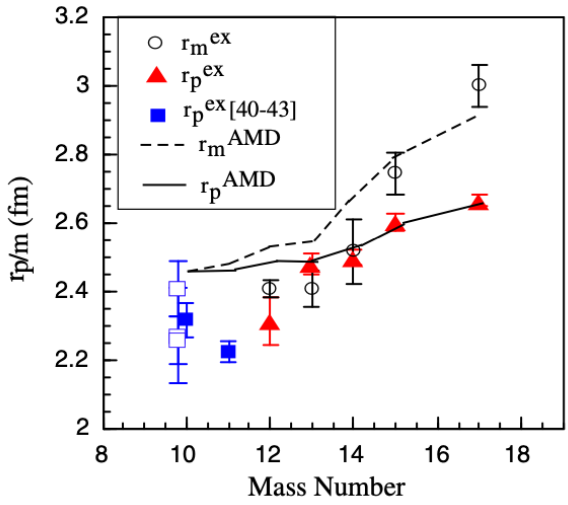

Figure 1.9: The proton radii (r_p) and rms matter radii (r_m) of $^{12-17}$B. [25]

Chapter 2

Methods

In this chapter, the methods used in this research are explained. First, Coulomb dissociation is introduced as a method to research the halo structure of ^{17}B. For the part of it, equivalent photon method as a tool for investigating the soft $E1$ excitation of ^{17}B is described. The $E1$ reduced transition probability $B(E1)$ and the geometrical information which is related to dineutron correlation can be obtained. Next, for extracting the Coulomb dissociation cross section from experimental data, the subtraction of nuclear breakup component is explained. Finally, the invariant mass method for the reconstruction of experimental data is explained.

2.1 Coulomb Dissociation

Coulomb dissociation is breakup reaction from excited stated by Coulomb excitation. Figure 2.1 shows the scheme of the Coulomb dissociation of ^{17}B used in this research. When nuclei incident into the high-Z target like lead, the projectile is excited by the electric field of target. When the final state is above the decay threshold, the Coulomb dissociation occurs.

2.1.1 Equivalent Photon Method

Equivalent photon method[11][12][13] is a powerful tool for investigating Coulomb excitation/dissociation in terms of the virtual photon. Under the equivalent photon method, Coulomb dissociation cross section σ_{CD} can be described with the photon absorption cross section $\sigma_{\gamma}^{E1}(E_x)$

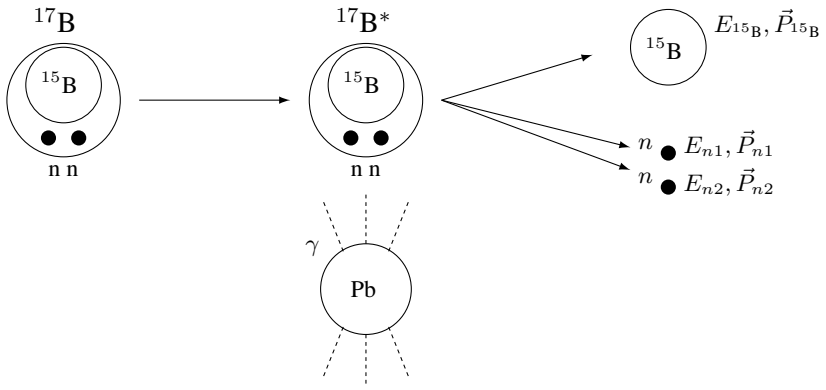

Figure 2.1: Schematic representation of Coulomb dissociation of ^{17}B. The ^{17}B is induced to Pb target and excited by virtual photon made from electric magnetic field by relativistic movement between ^{17}B and Pb target. The excited ^{17}B is dissociated into ^{15}B and two neutrons. The E and $\vec{P}$ are represent total energy and momentum of each fragment respectively.

and the virtual photon number $N_{E1}(E_x)$ as

$$\frac{d\sigma_{CD}}{dE_x} = \frac{N_{E1}(E_x)}{E_x}\sigma_\gamma^{E1}(Ex), \tag{2.1}$$

where E_x is the excitation energy of nuclei, $N_{E1}(E_x)$ is the virtual photon number produced by $E1$ transition. And the photon absorption cross section σ_γ^{E1} can directly be related to the $E1$ reduced transition probability $dB(E1)/dE_x$ as

$$\sigma_\gamma^{E1} = \frac{16\pi^3}{9\hbar c}E_x\frac{dB(E1)}{dE_x}. \tag{2.2}$$

Then, the Coulomb dissociation cross section is written as

$$\frac{d\sigma_{CD}}{dE_x} = \frac{16\pi^3}{9\hbar c}N_{E1}(E_x)\frac{dB(E1)}{dE_x}. \tag{2.3}$$

The virtual photon number for $E1$ transition N_{E1} is obtained by investigating the photon flux at an impact parameter b as

$$N_{E1}(E_x) = \int_b^\infty 2\pi b n_{E1}(E_x, b)db \tag{2.4}$$

$$= \frac{2}{\pi}Z_1^2\alpha\Big(\frac{c}{v}\Big)^2\Big[\xi K_0(\xi)K_1(\xi) - \frac{v^2\xi^2}{2c^2}(K_1^2(\xi) - K_0^2(\xi)\Big] \tag{2.5}$$

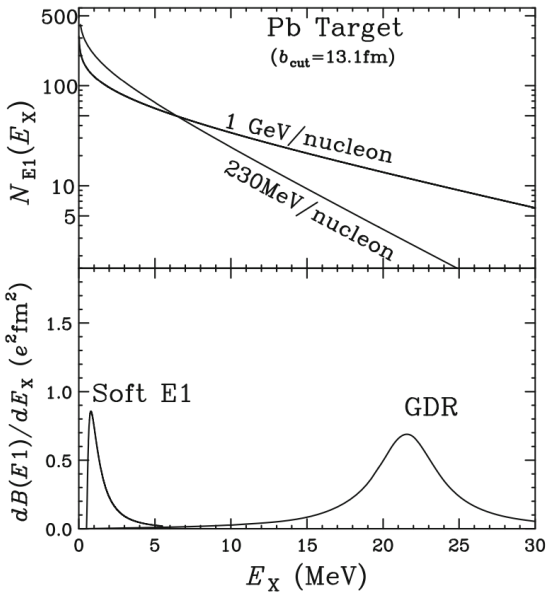

Figure 2.2: Virtual photon number $N_{E1}(E_x)$ spectra with the $dB(E1)/dE_x$ spectrum for halo nucleus[26]. The peak near 1 MeV shows the soft $E1$ excitation, while the peak in high energy region ($\sim$ 20 MeV) represents the giant dipole resonance.

$\xi = E_x b/\gamma v\hbar$
$E_\gamma = \omega\hbar$: Virtual photon energy
Z_1 : Atomic number of target
b : Impact parameter 1.3 ($17^{1/3} + 208^{1/3}$) = 11.048 fm
K_0, K_1 : Modified Bessel function of order zero and one
$\alpha = e^2/\hbar c$: Fine structure constants

In this experiment, we assumed the virtual photon energy E_γ is equal to excitation energy E_x of projectile. In Figure 2.2, the virtual photon number $N_{E1}(E_x)$ for $E1$ transition in the function of excitation energy E_x and the reduced $E1$ transition probability $dB(E1)/dE_x$ corresponding to energy region are shown. You can see there are two peaks corresponding to soft $E1$ excitation and giant dipole resonance respectively. Since the virtual photon number is exponentially decreasing with the excitation energy, the equivalent photon method is best suited for investigating the excitation in low energy region.

2.1.2 Geometry of Two Neutron Halo and Dineutron Correlation

Another information which can be extracted from $E1$ reduced transition probability is related with the geometrical value of the two neutron halo nucleus. By non-energy weighted cluster sum rule from Esbensen et at. [14], the $E1$ reduced transition probability $B(E1)$ in entire energy region can be written as

$$\begin{aligned} B(E1) &= \int_{-\infty}^{\infty} \frac{dB(E1)}{dE_x} dE_x \\ &= \frac{3}{\pi}\left(\frac{Ze}{A}\right)^2 \langle r_{c-nn}^2 \rangle, \end{aligned} \tag{2.6}$$

where $\langle r_{c-nn}^2 \rangle$ is a root mean square (rms) distance between the core nucleus and the two center of mass of two neutron. Furthermore, the distance between two neutrons $\langle r_{nn}^2 \rangle$ can be obtained from matter radius of halo and core nucleus in the three body model as [16][18],

$$\langle r_m^2 \rangle = \frac{A_c}{A}\langle r_m^2 \rangle_c + \frac{2A_c}{A^2}\langle r_{c-nn}^2 \rangle + \frac{1}{2A}\langle r_{nn}^2 \rangle \tag{2.7}$$

where A and $A_c (= A-2)$ are the mass number of halo and core nucleus respectively. $\langle r_m^2 \rangle$ and $\langle r_m^2 \rangle_c$ are the matter radius of halo and core nucleus respectively. In this research, for calculation, we use the value $\langle r_m^2 \rangle = 3.00(6)$ fm, $\langle r_m^2 \rangle_c = 2.75(6)$ fm from the rms radius of ^{17}B and ^{15}B respectively [25]. $\langle r_{nn}^2 \rangle$ is the distance between two neutrons. Finally, the opening angle between two neutrons $\langle \theta_{nn} \rangle$ can be obtained as,

$$\cos\frac{\theta_{nn}}{2} = \frac{r_{c-nn}}{\sqrt{r_{c-nn}^2 + \frac{r_{nn}^2}{4}}}. \tag{2.8}$$

2.2 Contribution of Nuclear Breakup

For evaluating the $B(E1)$ value, we need to extract only the Coulomb dissociation component from the experimental data. In this research, we used Γ factor method to remove the contribution of nuclear breakup component from lead target. For extracting the Coulomb dissociation cross section $\sigma(CD)$, we subtract the reaction cross section with the carbon target scaled by Γ factor from the one with the lead target. Using this method, we can write the Coulomb dissociation cross section

as follows.

$$\sigma_{CD} = \sigma(\mathrm{Pb}) - \Gamma\sigma(\mathrm{C}), \tag{2.9}$$

$\sigma(\mathrm{C})$ and $\sigma(\mathrm{Pb})$ are the reaction cross section with carbon and lead target respectively. Γ is the ratio of the reaction cross section with lead target to the one with carbon target. The Γ factor can be obtained from the geometry between the projectile and target nucleus as,

$$\Gamma_{\mathrm{min}} = \frac{R_{\mathrm{Pb}} + R_{^{17}\mathrm{B}}}{R_{\mathrm{C}} + R_{^{17}\mathrm{B}}} = \frac{A_{\mathrm{Pb}}^{1/3} + A_{^{17}\mathrm{B}}^{1/3}}{A_{\mathrm{C}}^{1/3} + A_{^{17}\mathrm{B}}} = 1.75 \tag{2.10}$$

$$\Gamma_{\mathrm{max}} = \frac{R_{\mathrm{Pb}}}{R_{\mathrm{C}}} = \frac{A_{\mathrm{Pb}}^{1/3}}{A_{\mathrm{C}}^{C}} = 2.59 \tag{2.11}$$

In this experiment, we used $\Gamma = 2.385$ value from calculation including the consideration of incident energy of ^{17}B at the middle of target (270 MeV/u)[27].

2.3 Invariant Mass Method

To reconstruct the excited state of ^{17}B at target, invariant mass method is used. Since ^{17}B has no bound excited state and its two neutron separation energy S_{2n} is very small, the dissociation process occurs very quickly. In this case, the invariant mass method is a useful tool to reconstruct the intermediate excited state of the system by measuring the momentum and energy of all of the fragments. The invariant mass of the excited state M^* is defined as

$$M^* = \sqrt{\left(\sum_i E_i\right)^2 - \left(\sum_i \vec{P}_i\right)^2} \tag{2.12}$$

where E_i and $\vec{P}_i$ are the energy and momentum of the fragment i respectively. In this experiment, the excited state of ^{17}B is reconstructed by measuring the momentum and energy of ^{15}B and two neutrons. The relative energy E_{rel} between ^{15}B and two neutron can be written with the invariant mass as

$$E_{rel} = M(^{17}\mathrm{B}^*) - (m_{^{15}\mathrm{B}} + m_n + m_n) \tag{2.13}$$

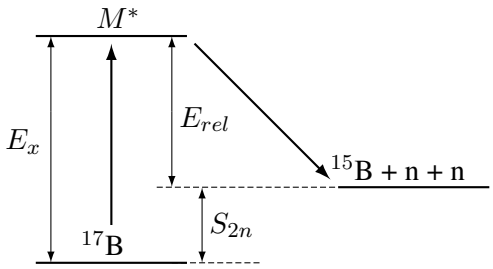

Figure 2.3: Schematic representation of the invariant mass method

where $m_{^{15}\mathrm{B}}$, m_n and m_n are the mass of ^{15}B and two neutrons respectively. The relative energy E_{rel} is related to the excitation energy E_x of ^{17}B and neutron separation energy S_{2n} as

$$E_{rel} = E_x - S_{2n} \tag{2.14}$$

Figure 2.3 shows the schematic representation of the invariant mass method.

Chapter 3

Experiment

This chapter describes the experimental setup in this study. The experiment is performed at Rare Isotope Beam Factory (RIBF) at RIKEN Nishina Center [28]. A primary ^{48}Ca beam is produced by the RIKEN accelerator complex and delivered to the BigRIPS separator [29][30][31]. The BigRIPS separator produced the ^{17}B secondary beam which bombarded on the lead and carbon targets in front of the SAMURAI (Superconducting Analyzer for MUlti-particles from Radioisotope beams) spectrometer[32]. After the reaction at the target, the fragments ^{15}B and two neutrons are detected by detectors at SAMURAI system.

3.1 Beam Information

The primary beam was accelerated by the SRC, RIBF. By accelerating ^{48}Ca to 345 MeV/u and bombarding it on a thick Be target (30mm), a secondary beam was produced. The characteristics of the primary beam is in Table 3.1.

Primary beam	Beam energy	Beam intensity	primary Target
^{48}Ca	345 MeV/u	210 pnA	Be (30mm)

Table 3.1: Information of primary beam

The collision of the primary beam and the target created the secondary beam, including not only the purpose isotope of this experiment, ^{19}B, but also other neighboring isotopes. The main isotope used in this research is ^{17}B, which needed to be separated and identified through the BigRIPS separator. The identified ^{17}B was then transferred to SAMURAI, where it underwent Coulomb dis-

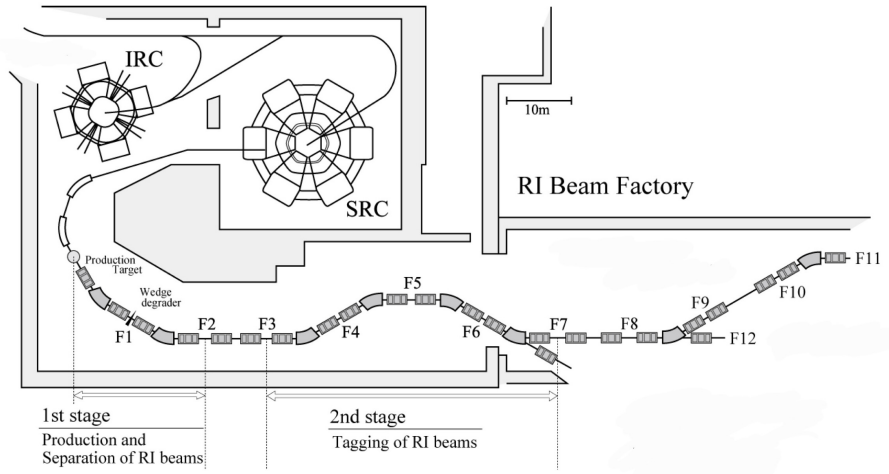

Figure 3.1: A top view of the BigRIPS separator [36]

sociation, the main objective of this research. Three different targets were used: C, Pb, and Empty. The details for the secondary beam ^{17}B is in Table 3.2.

Isotope	Target	Average energy at the middle of target
^{17}B	C (1.789 g/cm^2)	270 MeV/u
	Empty	275 MeV/u
	Pb (3.255 g/cm^2)	270 MeV/u

Table 3.2: Information of secondary beam

3.2 BigRIPS separator

The generated RI beams from SRC are separated by the BigRIPS separator. Figure 3.1 shows a top view of the BigRIPS separator. In the first stage of BigRIPS separator, the RI beam separated by dipole magnet with slit and wedge-shaped degrader located at F1 focal plane. In the dipole magnet, the rigidity of a particle can be written as following eq (3.1).

$$B\rho = v \cdot \frac{A}{Z} \tag{3.1}$$

The velocity of the secondary beam is almost same regardless of the nuclei so that it can be possible to choose specific A/Z by adjusting the slit to filter only some $B\rho$ value. After that, the wedge-shaped degrader makes the beam energy depends on the Z so that even same A/Z nuclei can be separated. Table 3.3 shows the BigRIPS separator setup for this experiment.

Location	Slit[mm]	Degrader / Detector
F0		Be target (30mm)
F1	$\pm$120	Al wedge degrader (15mm)
F2	L: 10 R: 7	
F3		Plastic Scintillator (3mm)
F5	$\pm$120	Beam Proportional Chamber
F7	$\pm$120	Plastic Scintillator (3mm)
F8	$\pm$170	
F12	$\pm$170	

Table 3.3: BigRIPS separator setup for Dayone experiment [36]

In the second stage, the RI beam is identified using TOF-Bρ-ΔE method. Detector information at BigRIPS will be described as following.

3.2.1 Plastic Scintillator

At focal plane F3, F7 and F13 in BigRIPS beam line, plastic scintillators are located for measuring the time of flight (TOF) of secondary beam. In F3 and F7, plastic scintillator with 3mm thickness is located and at F13 there are two scintillators, SBT1 and SBT2, with 0.5mm thickness. The flight length between F7 and F13 (Average point of SBTs) is 36.62 m. Table 3.4 shows the information of plastic scintillators at F3, F7, and F13.

Location	Thickness	Distance from target upstream
F3	3mm	86.05 m
F7	3mm	39.48 m
F13-1	0.5mm	2.90 m
F13-2	0.5mm	2.82 m

Table 3.4: Information of plastic scintillators at F3, F7, F13

3.3 SAMURAI

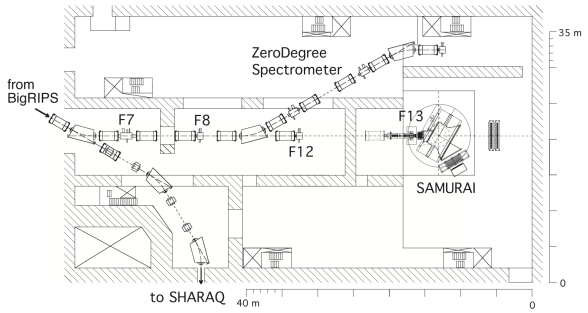

Figure 3.2: A top view of the beam line from BigRIPS to SAMURAI spectrometer[35]

The SAMURAI spectrometer is designed for kinematically complete experiment such as invariant mass spectroscopy[34]. Figure 3.2 and 3.3 shows a top view of the SAMURAI spectrometer. SAMURAI system includes Beam proportional chamber (BPC) for $B\rho$ measurement at F5, and two drift chambers (BDC1, BDC2) for tracking the secondary beam particle. After the reaction at secondary target, charged fragment bent by SAMURAI superconducting magnet and detected by two drift chambers (FDC1, FDC2) and one plastic scintillator (HODF). Finally the neutron detector array NEBULA is located at the end of extended beam line for neutron detection. The detailed information of each detector is described as following.

3.3.1 BPC (Beam Proportional Chamber)

BPC is Multi Wire Proportional Chamber (MWPC) located at F5 focal plane which is used for measuring the position of beam. The purpose of BPC is tagging magnetic rigidity and momentum of secondary beam. Figure 3.4 shows the schematic view of BPC and Table 3.5 shows the parameter of BPC.

Effective Area	(H)240mm $\times$ (V)150mm
Configuration	XX (2 Planes)
number of wire	64 $\times$ 2 = 128
Wire Pitch	4mm
Gas	i–C_4H_{10} at 50 torr

Table 3.5: Parameter of BPC (Beam Proportional Chamber) [32]

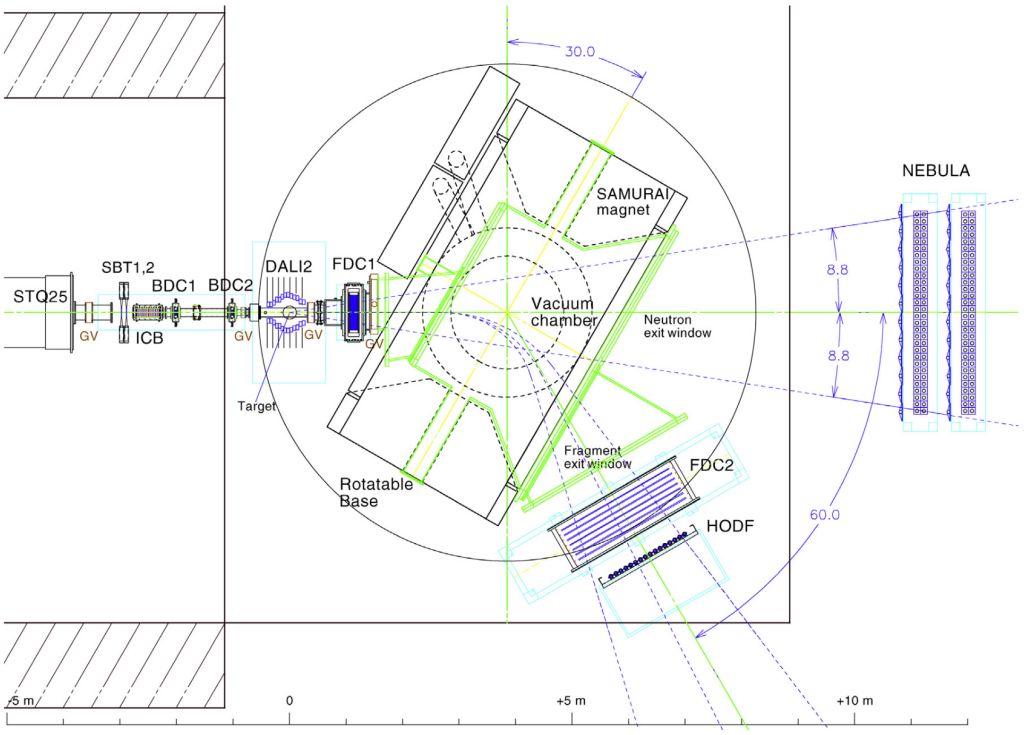

Figure 3.3: A top view of the SAMURAI spectrometer[32]

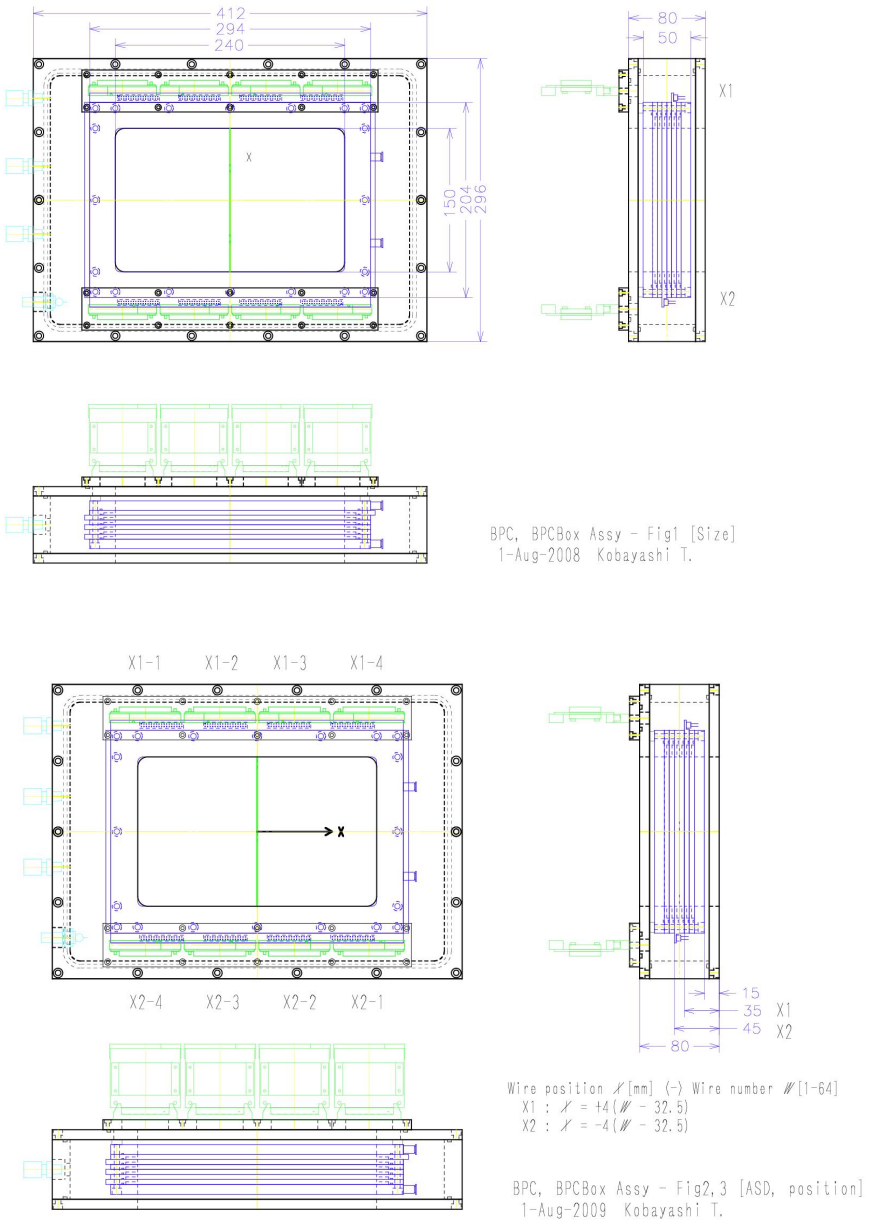

Figure 3.4: Schematic view of BPC (Beam Proportional Chamber) [32]

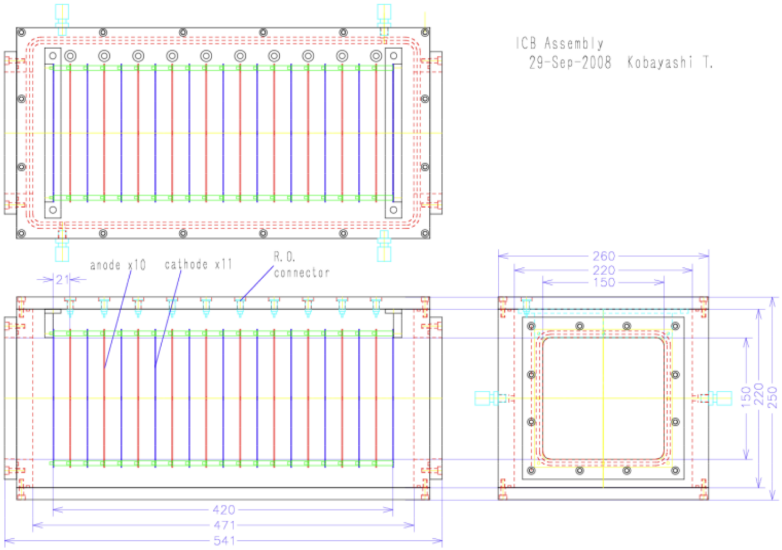

Figure 3.5: Schematic view of ICB (Ion Chamber for Beam) [32]

3.3.2 ICB (Ion Chamber for Beam)

The ICB is multi-layer ionization chamber for measuring the energy loss (ΔE) of secondary beam. Using P10 gas at 1 atm, the energy loss of secondary beam can be measured. Figure 3.5 shows the schematic view of ICB and Table 3.6 shows the parameter of ICB.

Effective Area	(H)140mm × (V)140mm × (D)420mm
Configuration	10 anodes and 11 cathodes
Anode-cathode gap	21mm
Gas	P10 at 1 atm
Distance from target upstream	4.76 m

Table 3.6: Parameter of ICB (Ion Chamber for Beam) [32]

3.3.3 BDC1, BDC2 (Beam Drift Chamber)

Before target, there are two Beam drift chamber for reconstructing the trajectory of secondary beam. Using the trajectory information, the position of secondary beam at target can be calculated. In this experiment, each BDC box is filled with i–C_4H_{10} gas at 100 torr. Figure 3.6 shows the schematic view of BDC and Table 3.7 shows the parameter of BDC.

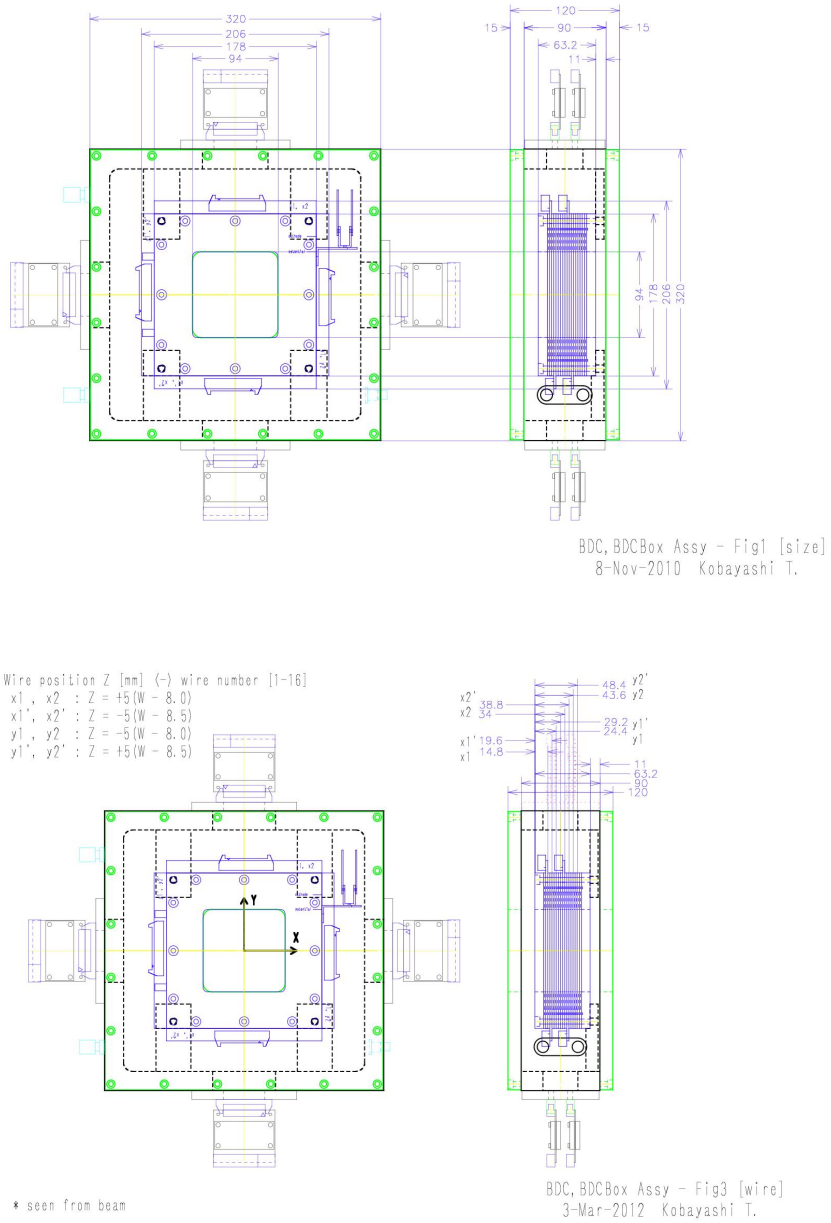

Figure 3.6: Schematic view of BDC (Beam Drift Chamber) [32]

Effective Area	(H)80mm × (V)80mm
Configuration	$XX'YY'XX'YY'$ (8 planes)
Number of Wire	16 × 8 = 128
Wire Pitch	5mm
Gas	i–C_4H_{10} at 100 torr
Distance from target upstream	(BDC1) 2.03 m (BDC2) 1.03 m

Table 3.7: Parameter of BDC (Beam Drift Chamber) [32]

3.3.4 DALI2

DALI2 (Detector Array for Low Intensity radiation 2) is a NaI(Tl) detector array for γ-ray spectroscopy[33]. It is consisted of 140 NaI(Tl) crystals surrounding the secondary target. The γ-ray emitted from the reaction at the target can be detected by DALI2.

3.3.5 SAMURAI Magnet

SAMURAI Magnet is a superconducting dipole magnet for bending the trajectory of charged fragment. The maximum field of SAMURAI magnet is 3.1 T and the maximum current is 563 A. Table 3.8 shows the parameter of SAMURAI magnet.

Type	Superconducting dipole magnet
Magnet Pole	ϕ 2m (0.88 m gap)
Maximum field	3.1 T
Maximum current	563 A

Table 3.8: Parameter of SAMURAI Magnet [32]

3.3.6 FDC1, FDC2 (Forward Drift Chamber)

After target, there are two forward drift chamber (FDC1, FDC2) for reconstructing the trajectory of charged fragment. Using the trajectory information, the rigidity of charged fragment at target can be calculated. In this experiment, FDC1 is filled with i–C_4H_{10} gas at 50 torr and FDC2 is filled with He + 50% C_2H_6 gas at 1 atm. Figure 3.7 and 3.8 show the schematic view of FDC1 and FDC2. And Table 3.9 and 3.10 show the parameter of FDC1 and FDC2.

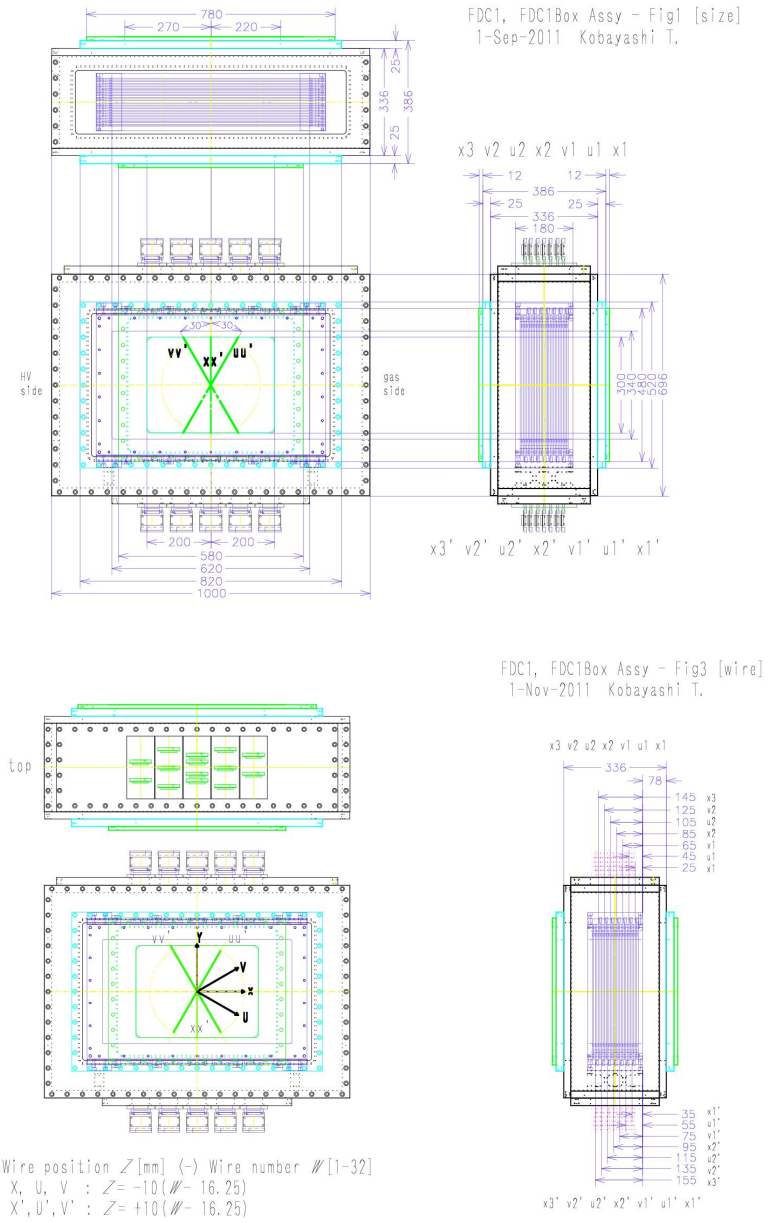

Figure 3.7: Schematic view of FDC1 (Forward Drift Chamber 1) [32]

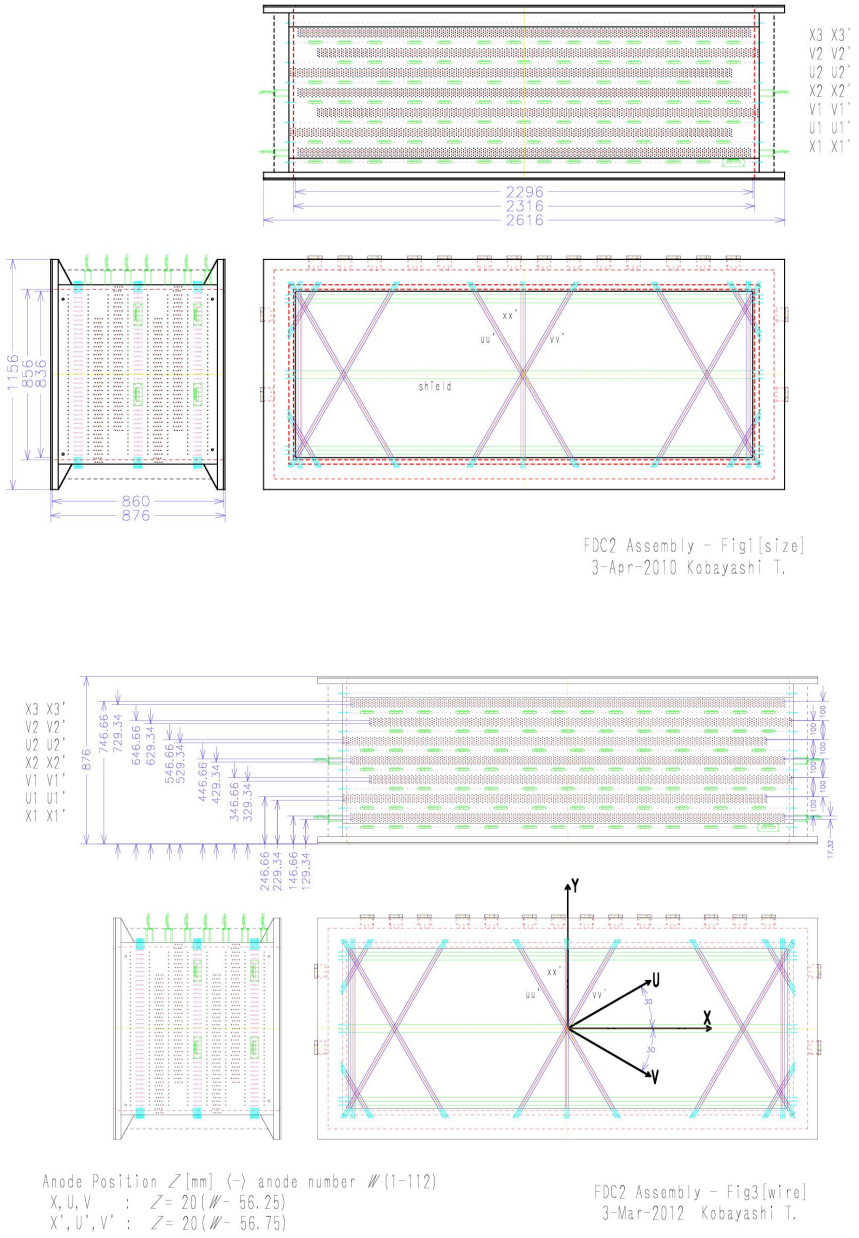

Figure 3.8: Schematic view of FDC2 (Forward Drift Chamber 2) [32]

Effective Area	(H)400mm × (V)300mm × (D)180mm
Configuration	$XX'UU'VV'XX'UU'VV'XX'$ (14 planes)
Number of Wire	32 × 14 = 448
Wire Pitch	10mm
Gas	i–C_4H_{10} at 50 torr
Distance from target upstream	1151.38 mm

Table 3.9: Parameter of FDC1 (Forward Drift Chamber 1) [32]

Effective Area	(H)2296mm × (V)836mm × (D)860mm
Configuration	$XX'UU'VV'XX'UU'VV'XX'$ (14 planes)
Number of Wire	112 × 14 = 1568
Wire Pitch	20mm
Gas	He + 50% C_2H_6 at 1 atm

Table 3.10: Parameter of FDC2 (Forward Drift Chamber 2) [32]

3.3.7 HODF (HODoscope for Fragment)

The plastic scintillator HODscope is located behind FDC2 for measuring the time of flight (TOF) and energy loss of charged fragment. HODF is consisted of 16 modules of plastic scintillator. Table 3.11 shows the parameter of HODF and Figure 3.9 shows the schematic view of HODF.

Effective Area	(H)1600mm × (V)1200mm × (D)10mm
Module	(H)100mm × (V)1200mm × (D)10mm
Configuration	16 module/layer × 1 layers

Table 3.11: Parameter of HODF (HODscope for Fragment) [32]

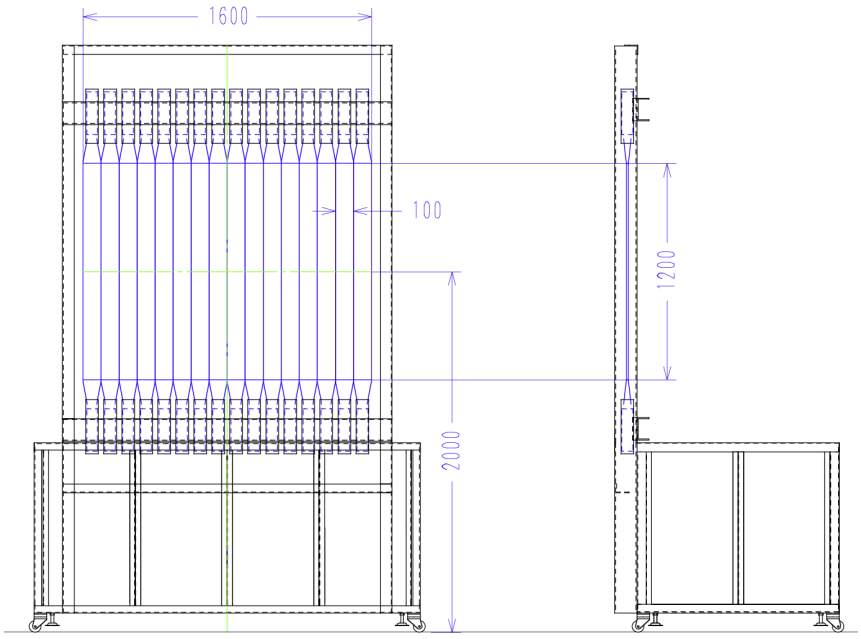

Figure 3.9: Schematic view of HODF (HODscope for Fragment) [32]

3.3.8 NEBULA

NEBULA (NEutron detection system for Break up of Unstable nuclei with Large Acceptance) is a neutron detector array located at the end of the extended beam line. NEBULA is consisted of 120 plastic scintillators for neutron detection and 24 plastic scintillators for veto. By NEBULA, we can reconstructed the neutron momentum vector from the target. Figure 3.10 shows the schematic view of NEBULA and Table 3.12 shows the parameter of NEBULA.

3.3.9 Geometry Information of SAMURAI Setup

Figure 3.11 shows the geometry information of SAMURAI setup[36].

Neutron detector	
Effective aria	(H)3600mm × (V)1800mm
Module	(H)120mm × (D)120mm × (V)1800mm
Configuration	30 module/layer × 4 layers
Veto detector	
Effective area	(H)3800mm × (V)1900mm
Module	(H)320mm × (D)10mm × (V)1900mm
Configuration	12 module/layer × 2 layers

Table 3.12: Parameter of NEBULA [32]

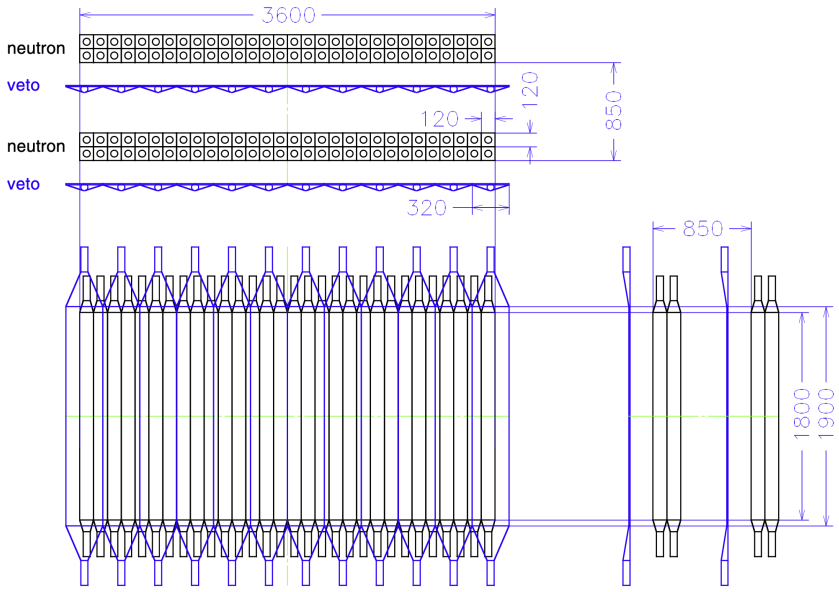

Figure 3.10: Schematic view of NEBULA [32]

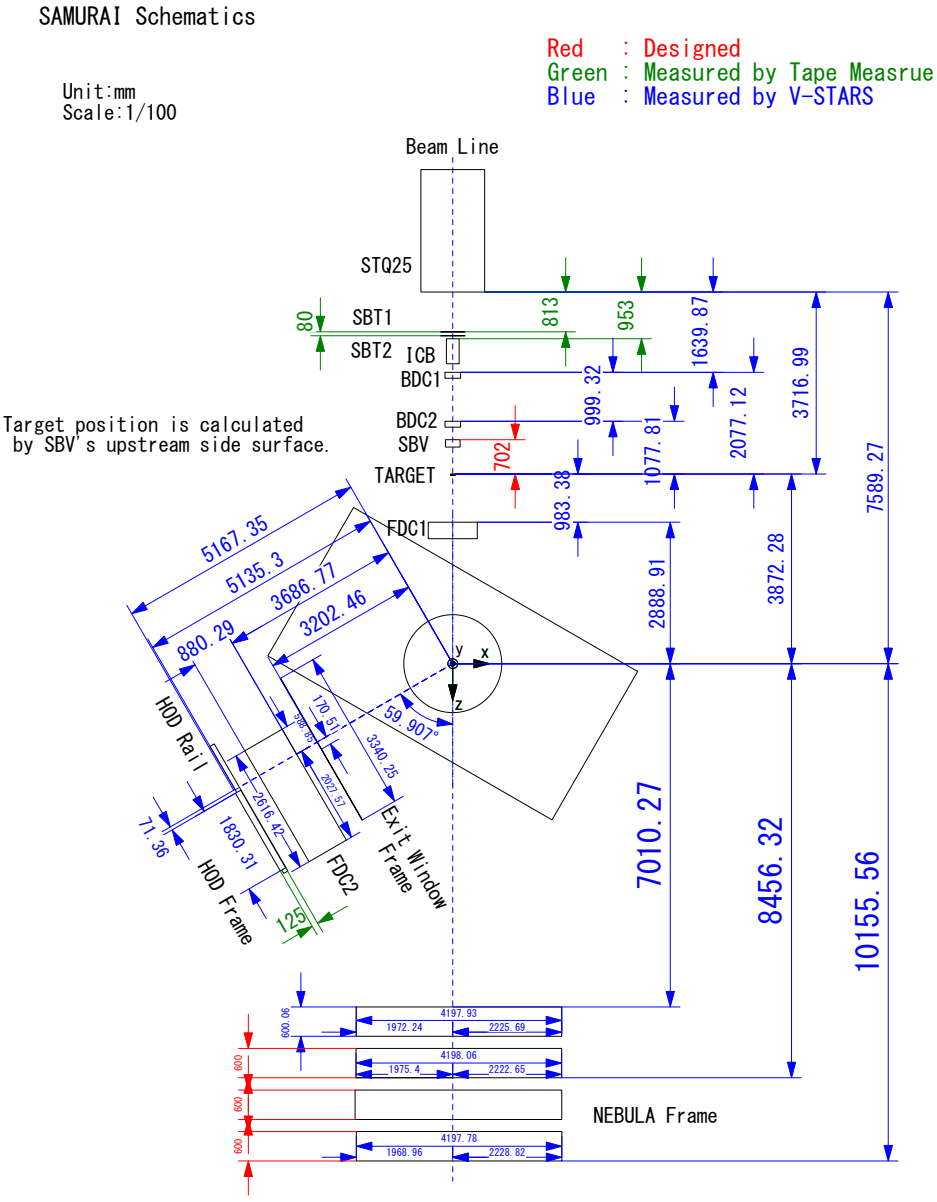

Figure 3.11: Geometry information of SAMURAI setup [36]

3.4 Run Summary

In this thesis, the data from the following runs are used for the data analysis. The run number, target, trigger condition, and note are shown in Table 3.13.

Run number	Target	Trigger	Note
394 - 404	C (1.789 g/cm^2)	DSB(1/20) $\cup$ (B $\cap$ N) $\cup$ D(1/1)	
405 - 409	Empty	DSB(1/20) $\cup$ (B $\cap$ N) $\cup$ D(1/1)	
410 - 427	Pb (3.255 g/cm^2)	DSB(1/20) $\cup$ (B $\cap$ N) $\cup$ D(1/1)	
428, 429, 431	Pb (3.255 g/cm^2)	DSB(1/1)	F5 slit $\pm$1mm
430	Pb (3.255 g/cm^2)	DSB(1/1)	F5 slit $\pm$5mm

Table 3.13: Run summary for experiment[36]

3.5 Electronics

3.5.1 Data Acquisition System and Trigger condition

There are three trigger conditions used in this experiment: DSB, B $\cap$ N, B $\cap$ N, B $\cap$ D. DSB (Down Scale Beam) trigger means the trigger rate is reduced with the down scale factor. In this research, the physics data set is collected with the down scale factor 1/20. B $\cap$ N (Beam $\cap$ NEBULA) trigger means the coincident between the beam trigger and the NEBULA trigger. B $\cap$ D (Beam $\cap$ DALI) trigger means the coincident between the beam trigger and the DALI trigger. The logic diagrams for beam, NEBULA and DALI trigger condition are shown in Figure 3.12, 3.13, and 3.14.

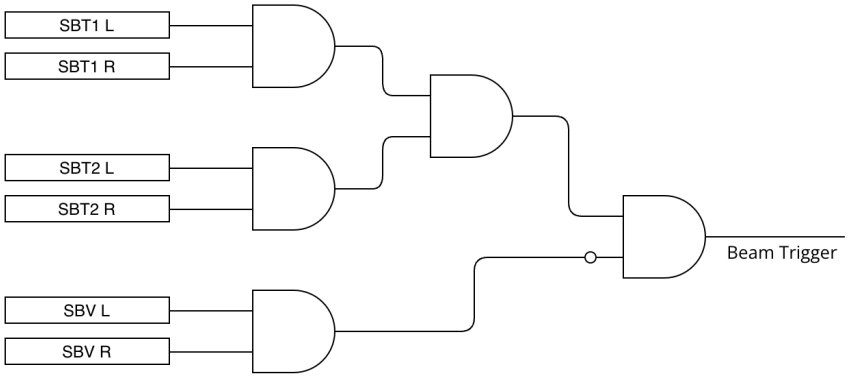

Figure 3.12: Logic diagram for beam trigger

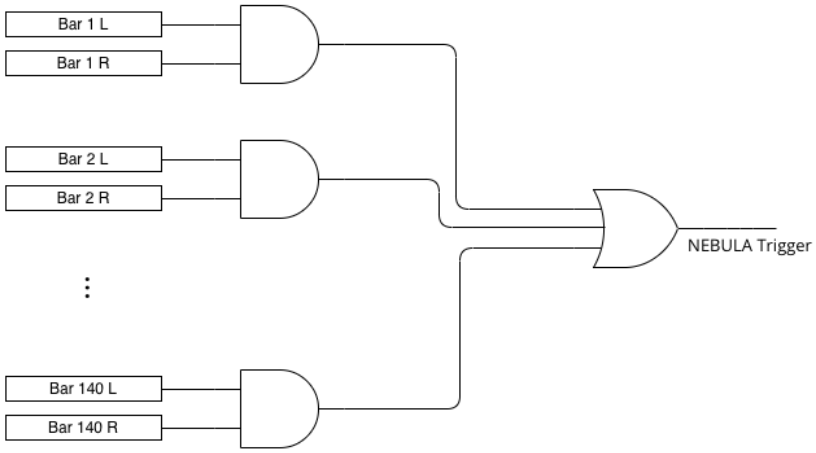

Figure 3.13: Logic diagram for NEBULA trigger

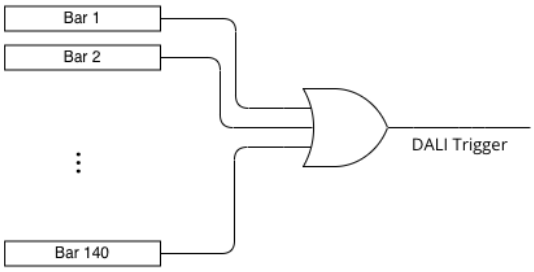

Figure 3.14: Logic diagram for DALI trigger

3.5.2 Live Time

The DAQ readout rate is limited by the dead time of the DAQ sub-system and the dead time depends on the trigger condition and the target. Figure 3.14 shows the live time of each reaction trigger for the live time correction of cross section.

Run number	target	DSB	B ∩ N, B ∩ D
394 - 404	C	0.843	0.815
405 - 409	Empty	0.890	0.854
410 - 427	Pb	0.861	0.831

Table 3.14: Live time of each reaction trigger

Chapter 4

Data Analysis

In the analysis of experimental data, the primary goal is to extract a differential cross section for Coulomb dissociation of ^{17}B as a function of relative energy between ^{15}B and two neutrons. To achieve the goal, I will describe the procedure of identifying the secondary beam of ^{17}B, and selecting events involving the fragment ^{15}B and two neutrons. The flow of the data analysis is as follows.

1. Select the event containing ^{17}B beam by beam particle identification
2. Select the event containing ^{15}B fragment by fragment particle identification
3. Select the event containing two neutrons by cross-talk analysis
4. Extract the $2n$ removal cross section of the $^{17}\mathrm{B} \rightarrow {}^{15}\mathrm{B} + 2n$ reaction
5. Reconstruct invariant mass at target and obtain the relative energy spectrum

4.1 Secondary Beam Particle Identification

The identification of the ^{17}B secondary beam was performed using the TOF-$B\rho$-ΔE method. Time of Flight (TOF) is obtained from time difference between scintillator at F7 and F13, $B\rho$ is calculated from the beam passing x position at F5, and ΔE is measured from ionization chamber ICB. A/Z and Z of the secondary beam is driven by the following equation.

$$\beta_{\mathrm{TOF_{F7\text{-}F13}}} = L(\text{F7-F13})/(\mathrm{TOF_{F7\text{-}F13}} \times c) \tag{4.1}$$

$$\beta_{\mathrm{F5}} = f(\mathrm{TOF_{F7\text{-}F13}}) \tag{4.2}$$

$$A/Z = \frac{c \times B\rho_{\mathrm{F5}} \times \gamma_{\mathrm{F5}}}{m_u \times \beta_{\mathrm{F5}}} \tag{4.3}$$

$$\tag{4.4}$$

$$Z = \beta_{\mathrm{F7\text{-}F13}} \sqrt{\Delta E_{\mathrm{ICB}} \left\{ 0.307075 \cdot \Delta x \left(\frac{Z_{\mathrm{P10}}}{A_{\mathrm{P10}}} \right) \ln \left(\frac{2m_e c^2 \beta^2_{\mathrm{F7\text{-}F13}} \gamma^2_{\mathrm{F7\text{-}F13}}}{I_{\mathrm{P10}}} - \beta^2_{\mathrm{F7\text{-}F13}} \right) \right\}^{-1}} \tag{4.5}$$

L(F7-F13) is a distance between F7 and F13 scintillator, $f(\mathrm{TOF_{F7\text{-}F13}})$ is 2nd order polynomial function of TOF for fitting β_{F5}. ΔE_{ICB} is total energy loss at ICB and Z_{P10}, A_{P10} and I_{P10} are effective atomic number, effective mass number and mean excitation energy of P10 gas. Δx is a travel distance in ICB. The detail of each steps are described in following.

4.1.1 Time of Flight

The Time of Flight (TOF) is measured using the time difference between two plastic scintillators. In the present analysis, from the timing at F7 plastic scintillator (t_{F7}) and the ones from SBT1,2 at F13 (t_{SBT1}, t_{SBT2}), the $\mathrm{TOF_{F7-F13}}$ is obtained by following equation.

$$\mathrm{TOF_{F7\text{-}F13}} = \frac{t_{\mathrm{SBT1}} + t_{\mathrm{SBT2}}}{2} - t_{\mathrm{F7}} + \Delta t_{offset} \tag{4.6}$$

Δt_{offset} is the offset used to correct for the difference between the actual measured $\mathrm{TOF_{F7\text{-}F13}}$ and the calculated TOF value with the consideration of energy loss at the materials between F7 and F13. The calculated $\mathrm{TOF_{F7\text{-}F13}}$ value is 192.34 ns, and the corresponding Δt_{offset} value is 172.03 ns.

4.1.2 Magnetic Rigidity

Magnetic Rigidity $B\rho$ is derived by Beam Projection Chamber (BPC) located at F5 dispersive focal plane. The x position of a beam passing through F5 is measured by BPC, and the $B\rho$ is

calculated using the following equation.

$$B\rho = (1 + \frac{x}{D})B\rho_0 \tag{4.7}$$

with the rigidity of the central trajectory $B\rho_0$ is 8.780 Tm, and momentum dispersion D is 3300 mm/%.

4.1.3 Energy Loss

The energy loss ΔE is measured in the Ionize Chamber for Beam (ICB). The correlation between ΔE and Z can be obtained according to the simplified Bethe-Bloch's energy loss formula as follows.

$$\frac{\Delta E}{\Delta x} = 2\pi N_a r_e^2 m_e c^2 \rho_{\text{P10}} \left(\frac{Z_{\text{P10}}}{A_{\text{P10}}}\right)\left(\frac{Z^2}{\beta^2}\right)\left[\ln \frac{2m_e c^2 \beta^2 \gamma^2}{I_{\text{P10}}} - \beta^2\right] \tag{4.8}$$

with

$$2\pi N_a r_e^2 m_e c^2 \rho_{\text{P10}} = 0.307075 \text{ MeV cm}^2\text{g}^{-1} \tag{4.9}$$

N_a : Avogadro's number = 6.022 $\times$ 10^{23}
r_e : classical electron radius = 2.817 $\times$ 10^{-13} cm
m_e : electron mass = 0.511 MeV/c^2
ρ_{P10} : density of the P10 gas = 1.84 $\times$ 10^{-3} g/cm^3
Z_{P10} : effective atomic number of the P10 gas
A_{P10} : effective mass number of the P10 gas
I_{P10} : mean excitation energy of the P10 gas
β = v/c of the beam particle
γ = $1/\sqrt{1-\beta^2}$

In this formula, the density effect correction δ or shell correction C are skipped. Since the P10 gas is compound of 90% Ar and 10% CH_4, the mean excitation energy I_{P10} is calculated based on [38]. The travel distance in ICB, which is calculated as (total length of ICB) $\times$ (probability of each gas in P10) $\times$ (volume density).

$$\Delta x = 51 \times 0.9 \times 0.0016608 + 51 \times 0.1 \times 0.000667 \tag{4.10}$$

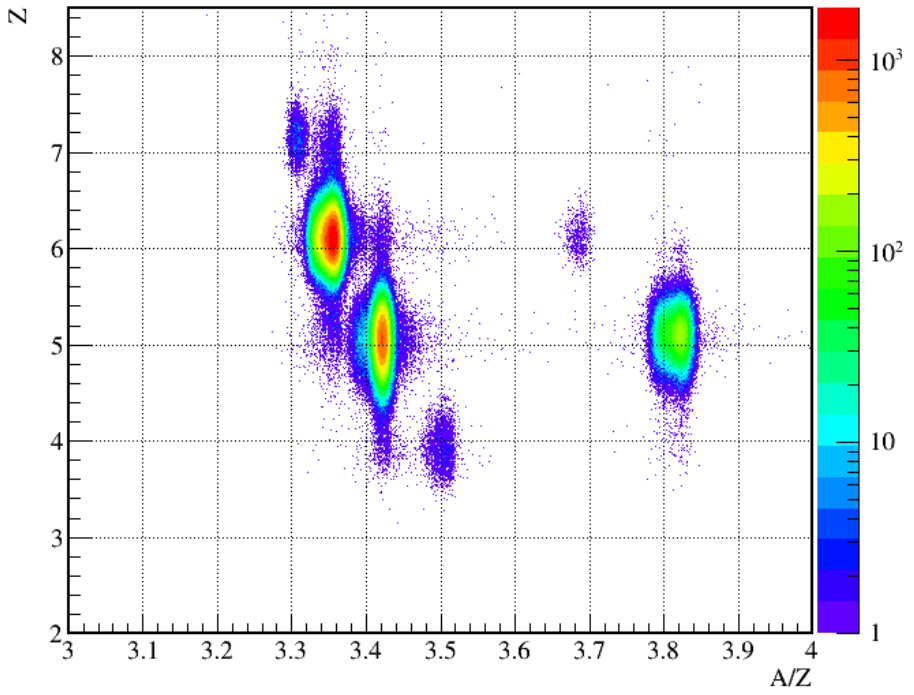

Figure 4.1: Beam particle identification of the secondary beam

4.1.4 Beam Particle Identification

Figure 4.1 shows the histogram of the particle identification of the secondary beam, showing Z versus A/Z. The total numbers of the secondary beam for each target is summarized in Table 4.1.

The gate condition for ^{17}B is as follows.

- DSB trigger
- effective area of target $x < \pm$ 35 mm and $y < \pm$ 35 mm
- $4.40 < Z < 5.69$ and $3.4 < A/Z < 3.44$

4.2 Beam Profile at Target

The beam profile at the target can be determined using the two drift chambers, BDC1 and BDC2, located upstream of the target. The incident position and angle at the target are obtained

Secondary Beam	Pb target	C target	Empty target
^{17}B	829586	756021	331445
^{19}B	160905	144243	63033
^{20}C	1675080	1483113	510410

Table 4.1: Statistic of secondary beam

from the beam positions at BDC1 and BDC2.

4.2.1 BDC Calibration

The BDC drift chamber is designed for tracking the incident particle. Beam particle trajectory is obtained by following procedure.

1. Obtain a drift time from TDC distribution.
2. Extract a hit position of each layer from STC (Space to Time Conversion) function.
3. Fit the trajectory with the linear function by the least-square method.

TDC (Time to Digital Converter) Distribution

The timing information of the BDC is obtained by TDC (Time to Digital Converter). In figure 4.2, the TDC distribution of BDC1 and BDC2 are shown. Since we used common stop mode to take a TDC data in this experiment, the drift time is,

$$t_{drift} = t_{max} - t_{\mathrm{TDC}} \tag{4.11}$$

where t_{max} is the maximum TDC value. This TDC distribution is obtained from run 431 with $\pm$ 5mm slit at F5.

STC (Space to Time Conversion) Function

The distance between hit position to an anode wire is given by space time conversion (STC) from the drift time. Assuming the uniform position distribution in each drift length cell as

$$\frac{dN}{dx} = const. \tag{4.12}$$

The STC function is derived by integrating the TDC distribution as,

$$\frac{dN}{dt} \cdot \frac{dt}{dx} = const. \tag{4.13}$$

$$dx = C \cdot \frac{dN}{dt} \cdot dt, \tag{4.14}$$

$$x(t) = C \cdot \int_{t_0}^{t} \frac{dN}{dt} dt \tag{4.15}$$

where, C is normalization factor, t_0 is the minimum drift time and t is the drift time from TDC distribution. The integration range of TDC for each BDC is shown in table 4.2. The upper and lower limit is determined by the TDC distribution. (Figure 4.2)

	Lower limit [ch]	Upper limit [ch]
BDC1	640	760
BDC2	630	750

Table 4.2: TDC integration ranges of BDC1 and BDC2

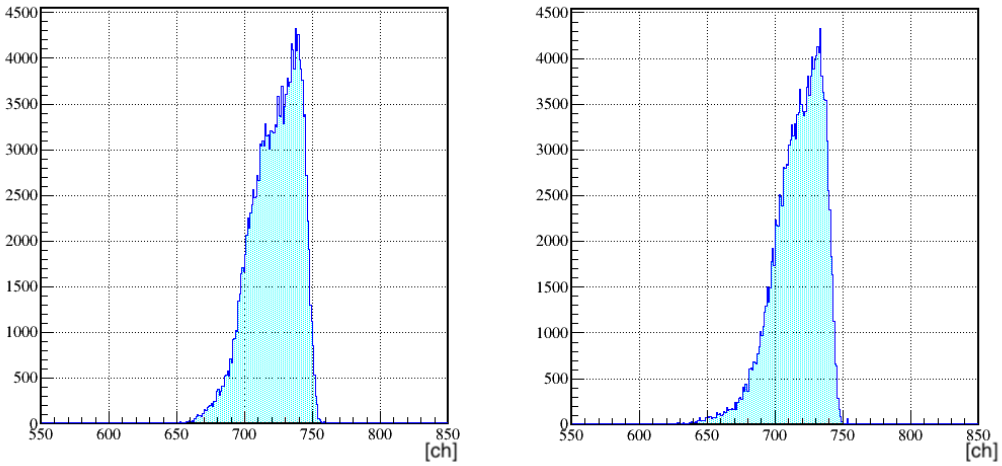

Figure 4.2: TDC Distribution of BDC1 (left) and BDC2 (right)

	σ_x [mm]	σ_y [mm]
BDC1	0.1340	0.1627
BDC2	0.1422	0.1743
	σ_a [rad]	σ_b [rad]
BDC1	0.01316	0.01330
BDC2	0.01396	0.01424

Table 4.3: Position and Angular Resolution of BDCs

Linear fitting of trajectory

After getting the STC function, the hit position of each layer is calculated from drift time as eq. (4.15). Now we can get the trajectory of beam particle by fitting the hit position with linear function. When fitting the trajectory, the least-square method is used. The least-square method is the method of finding the best fit of a set of hit positions by minimizing the χ^2 value. The χ^2 value is defined as,

$$\chi^2 = \sum_{i=1}^{N} \frac{(x_i - f(x_{fit}))^2}{\sigma_i^2} \tag{4.16}$$

where, x_i is the hit position of each layer, $f(x_{fit})$ is the position from fitting function, σ_i is the position resolution of each layer.

The resolution of BDCs

After tracking the trajectory, the resolution of BDCs can be evaluated by the tracking residue distribution. The tracking residue $x_{residue}$ is defined as,

$$x_{residue} = x_{trac} - x_{drift} \tag{4.17}$$

where x_{trac} is the calculated position from the trajectory and x_{drift} is the hit position of each layer. The tracking residue distribution of BDC1 and BDC2 are shown in Figure 4.3. The width of residue distribution for x and y direction are Δx = 0.2605 mm, Δy = 0.2632 mm respectively. From this, the position and angular resolution are calculated as described in the Appendix A. The result is described in table 4.3.

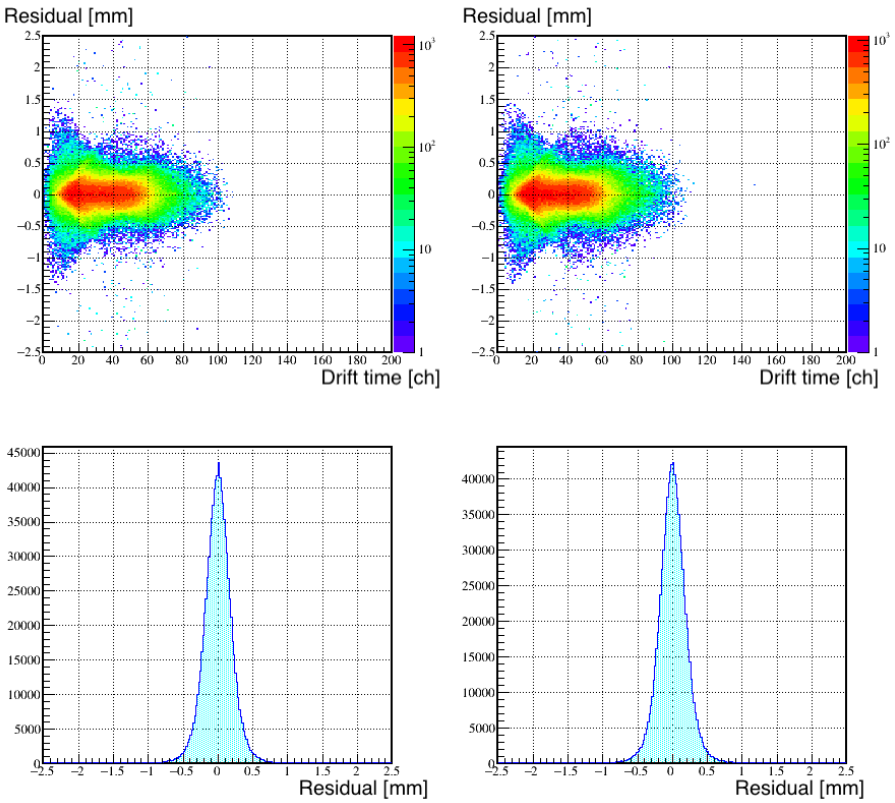

Figure 4.3: Tracking Residue Distribution of BDC1 (left) and BDC2 (right)

4.2.2 Beam Profile at Target

The beam profile at the target is obtained by using the position information from BDCs. The position information (x_{tgt}, y_{tgt}) and angle information (a_{tgt}, b_{tgt}) at the target are obtained as,

$$x_{\text{tgt}} = x_{\text{BDC1}} + \frac{(x_{\text{BDC2}} - x_{\text{BDC1}})}{L(\text{BDC1} - \text{BDC2})} \times L(\text{BDC1} - \text{tgt}) \tag{4.18}$$

$$y_{\text{tgt}} = y_{\text{BDC1}} + \frac{(y_{\text{BDC2}} - y_{\text{BDC1}})}{L(\text{BDC1} - \text{BDC2})} \times L(\text{BDC1} - \text{tgt}) \tag{4.19}$$

$$a_{\text{tgt}} = tan^{-1}\left(\frac{(x_{\text{BDC2}} - x_{\text{BDC1}})}{L(\text{BDC1} - \text{BDC2})}\right) \tag{4.20}$$

$$b_{\text{tgt}} = tan^{-1}\left(\frac{(y_{\text{BDC2}} - y_{\text{BDC1}})}{L(\text{BDC1} - \text{BDC2})}\right), \tag{4.21}$$

where the distance between BDCs is $L(\text{BDC1} - \text{BDC2}) = 999.32$mm, and the distance between BDC1 and the target is $L(\text{BDC1} - \text{tgt}) = 2017.13$mm. The beam profile at the target is shown in Figure 4.4.

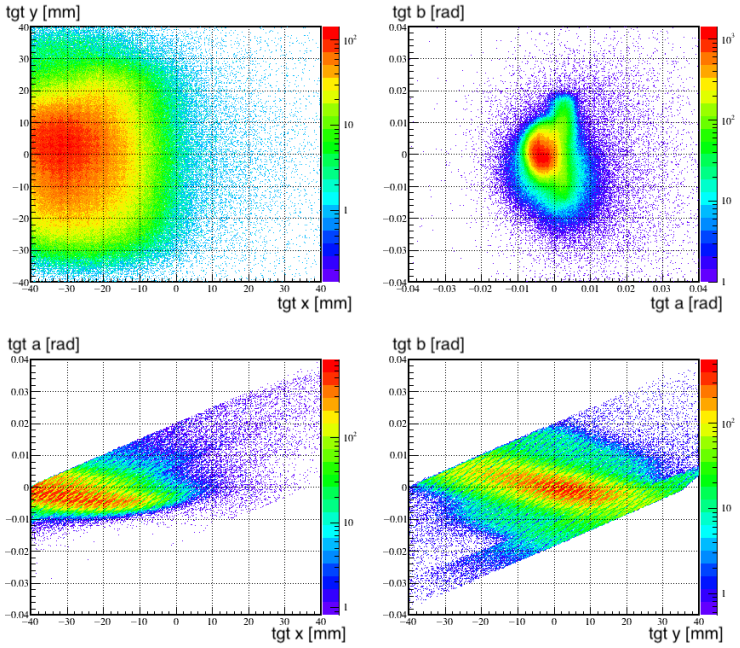

Figure 4.4: ^{17}B Beam profile at target

4.2.3 Position and Angular Resolution at Target

$$\Delta\theta_x^{\text{tgt}} = \Delta\left(\frac{x_{\text{BDC2}} - x_{\text{BDC1}}}{L(\text{BDC2} - \text{BDC1})}\right) = \frac{\sqrt{(\Delta x_{\text{BDC2}})^2 + (\Delta x_{\text{BDC1}})^2}}{999.32\text{mm}} = 0.196\text{mrad} \tag{4.22}$$

$$\Delta\theta_y^{\text{tgt}} = \Delta\left(\frac{y_{\text{BDC2}} - y_{\text{BDC1}}}{L(\text{BDC2} - \text{BDC1})}\right) = \frac{\sqrt{(\Delta y_{\text{BDC2}})^2 + (\Delta y_{\text{BDC1}})^2}}{999.32\text{mm}} = 0.239\text{mrad} \tag{4.23}$$

The position resolution at the target is

$$\Delta x_{\text{tgt}} = \sqrt{(\Delta x_{\text{BDC2}})^2 + (\Delta\theta_x^{\text{tgt}} \cdot L(\text{tgt} - \text{BDC2}))^2} = 0.24\text{mm} \tag{4.24}$$

$$\Delta y_{\text{tgt}} = \sqrt{(\Delta y_{\text{BDC2}})^2 + (\Delta\theta_y^{\text{tgt}} \cdot L(\text{tgt} - \text{BDC2}))^2} = 0.28\text{mm} \tag{4.25}$$

4.3 Charged Particle Identification

Charged particles are identified using the TOF-Bρ-ΔE method as same as the beam particle identification. Time of Flight is obtained from time difference between target and HODF, $B\rho$ is calculated from FDC1 and FDC2 positions and angles, and Z is calculated by HOD Q information. A/Z and Z is obtained by the following equation.

$$\beta_{\text{frag}} = L(\text{tgt - HODF})/(\text{TOF}_{\text{tgt - HODF}} \times c) \tag{4.26}$$

$$A/Z = \frac{c \times B\rho \times \gamma_{\text{frag}}}{m_u \times \beta_{\text{frag}}} \tag{4.27}$$

$$Z = p_0 + p_1(Q_{\text{HOD}} - p_2\frac{1}{\beta^2}) \tag{4.28}$$

L(tgt - HODF) is flight length from target to HODF. This is also calculated by a function of the positions and angles at FDC1 and FDC2 as the one for $B\rho$. The coefficient of Z calculation p_0, p_1, p_2 are obtained by linear fitting of HOD Q distribution. The detail of each steps will be described in following.

4.3.1 FDC Calibration

The tracking procedure of FDCs is same as BDC. The integration range of TDC for each FDC is shown in table 4.4 And the TDC distribution for determining the upper and lower limit are shown in Figure 4.5.

	Lower limit [ch]	Upper limit [ch]
FDC1	1300	1600
FDC2	500	1470

Table 4.4: TDC integration ranges of FDC1 and FDC2

The resolution of FDCs

The residue distributions of all plane of FDCs are shown in Figure 4.6. From this, the position and angular resolution are calculated as described in the Appendix A. The result is described in table 4.5.

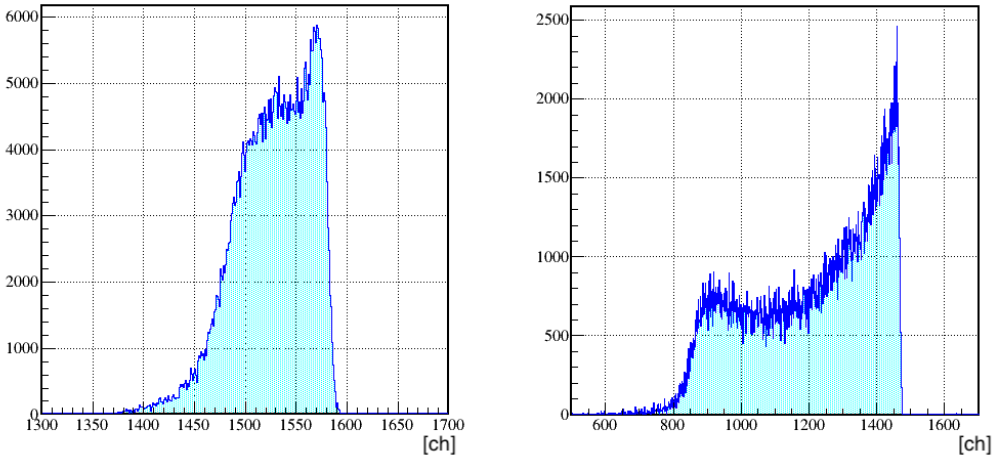

Figure 4.5: TDC Distribution of FDC1 (left) and FDC2 (right)

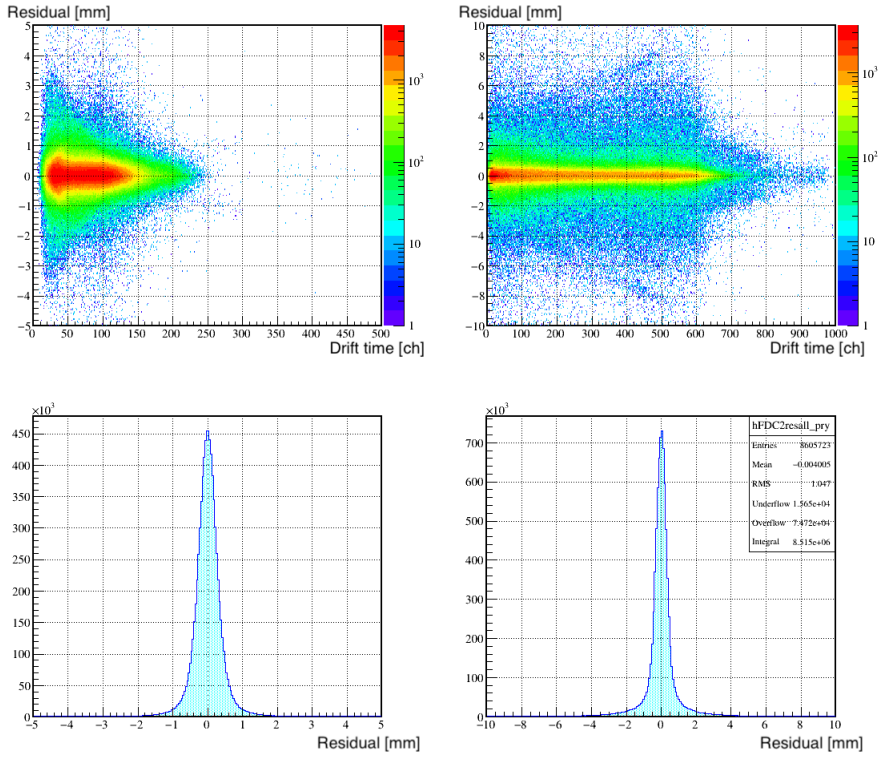

Figure 4.6: Tracking Residue Distribution of FDC1 (left) and FDC2 (right)

	Δx_0 [mm]	Δy_0 [mm]
FDC1	0.1239	0.2944
FDC2	0.1450	0.3443
	Δa_0 [rad]	Δb_0 [rad]
FDC1	0.00289	0.00948
FDC2	0.00068	0.00224

Table 4.5: Position and angular resolution of FDCs

The efficiency of FDCs

The efficiency of FDCs is evaluated by the tracking efficiency. The tracking efficiency is defined as the ratio of the number of events with a track at FDCs to the number of events with a hit at HODF. The definition of each efficiency can be written in following equation.

$$\epsilon_{\text{FDC1}} = \frac{N(\text{FDC1} \cap \text{HODF})}{N(\text{HODF})} \tag{4.29}$$

$$\epsilon_{\text{FDC2}} = \frac{N(\text{FDC2} \cap \text{HODF})}{N(\text{HODF})} \tag{4.30}$$

The efficiency of FDC1 and FDC2 of ^{15}B fragment for lead target is 96.0% and 99.9% respectively. The efficiency of FDC1 and FDC2 for carbon target is 93.1% and 99.9% respectively. And the efficiency of FDC1 and FDC2 for empty target is 98.9% and 99.9% respectively.

4.3.2 Magnetic Rigidity

The Brho of the charged particle is calculated from the positions and angles obtained from FDC1 and FDC2. The $B\rho$ is calculated by the following equation.

$$B\rho = f(x_{\text{FDC1}}, y_{\text{FDC1}}, a_{\text{FDC1}}, b_{\text{FDC1}}, x_{\text{FDC2}}, a_{\text{FDC2}}) \tag{4.31}$$

$$= \sum_i c_{1,i} a_i + \sum_i \sum_j c_{2,ij} a_i a_j + \sum_i \sum_j \sum_k c_{3,ijk} a_i a_j a_k + \cdots \tag{4.32}$$

$$= c_{1,0} x_{\text{FDC1}} + c_{1,1} y_{\text{FDC1}} + \cdots + c_{2,00} x_{\text{FDC1}}^2 + c_{2,01} x_{\text{FDC1}} y_{\text{FDC1}} + \cdots + c_{3,000} x_{\text{FDC1}}^3 + \cdots \tag{4.33}$$

The function of Bρ is extracted by using TMultiDimFit class in ROOT using a trajectory obtained from Geant4 simulation.

4.3.3 Time of Flight and Energy Loss

Time of Flight

Time of flight of charged particle is determined by the time difference between the HODF and the target. The time at target is determined by addition of the time at F13 and the time of flight from F13 to the target. The time of flight between F13 and the target is calculated with ^{17}B beam with Energy loss calculation considered the material between F13 and the target. The time of flight between HODF and target is defined by the following equation.

$$t_{\text{tgt}} = t_{F13} + tof_{\text{F13-tgt}} tof_{\text{HODF-tgt}} = t_{\text{HODF}} - t_{\text{tgt}} + \Delta t_{offset} \tag{4.34}$$

where t_{HODF} is timing information of HODF and Δt_{offset} is obtained by Geant4 simulation as same as Bρ analysis. The Δt_{offset} is defined as 112.53 ns.

Energy Loss

In case of fragment, the energy loss is obtained from the light output information of HODF scintillator. From the Bethe-Bloch formula, we assumed that

$$Z_{frag} \propto \beta_{frag}\sqrt{\Delta E} = \beta_{frag}\sqrt{Q_{\text{HODF}}}. \tag{4.35}$$

β_{frag} is obtained from the time of flight information and Q_{HODF} is the light output information of HODF. Because of the proportional relation between Z_{frag} and $\sqrt{Q_{\text{HODF}}}$, it is difficult to identify the fragment particle by only energy loss information. So first we gate the fragment particle by ^{17}B beam, and assumed that most of fragment came from ^{17}B should be ^{17}B itself. Then we can get coefficient for calculating the Z.

4.3.4 Fragment Particle Identification

The fragment particle identification is shown in figure 4.7 and 4.8. Figure 4.7 is the fragment particle identification of all events. Figure 4.8 is the fragment particle identification only from ^{17}B beam events. We selected the ^{15}B events with $4.735 < Z < 5.275$ and $2.95 < A/Z < 3.07$ and ^{13}B events with $4.735 < Z < 5.275$ and $2.58 < A/Z < 2.70$.

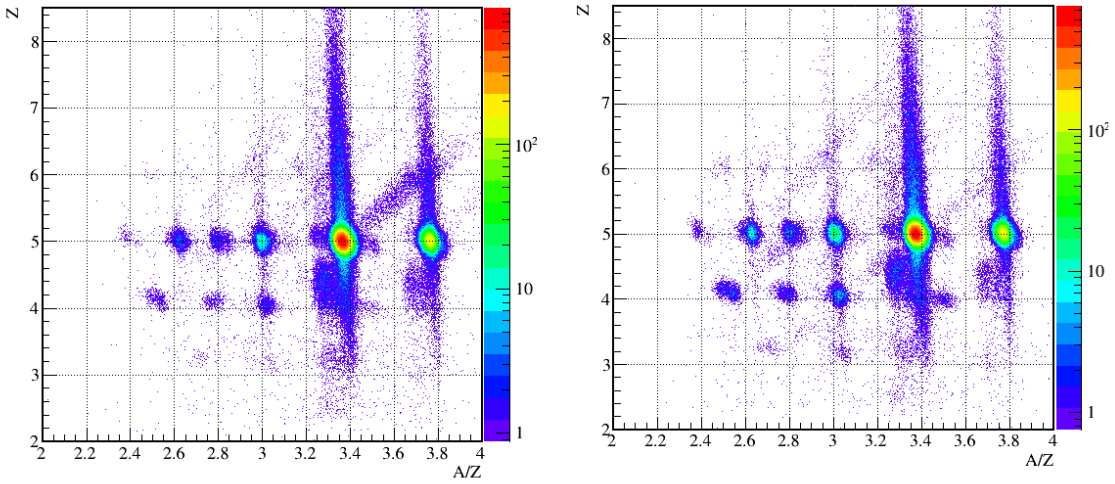

Figure 4.7: Fragment particle identification of all events at Pb target (left) and C target (right)

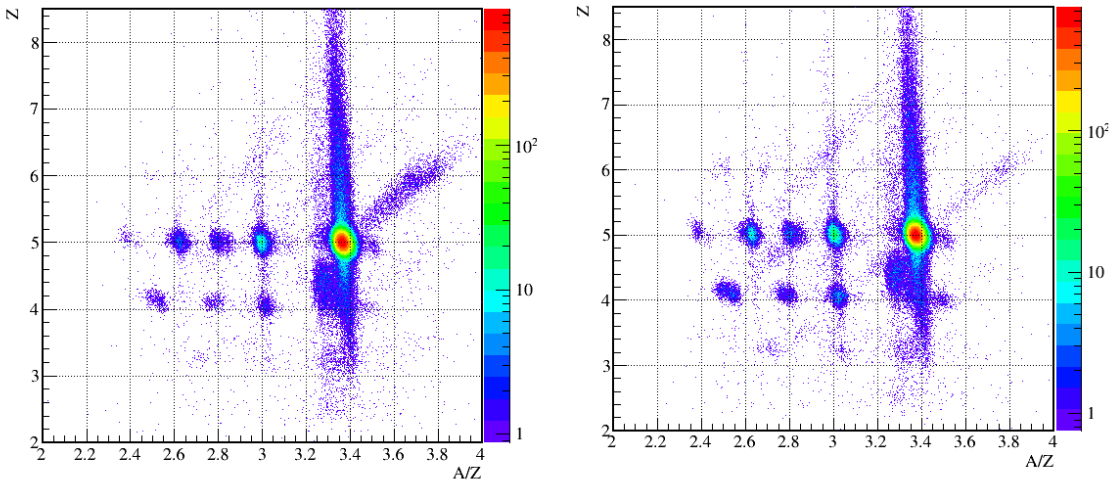

Figure 4.8: Same as Figure4.7 but gated by ^{17}B events at Pb target (left) and C target (right)

4.4 Analysis of Neutrons

In this experiment, neutrons emitted in the breakup reaction from the secondary beam ^{17}B are detected by the NEBULA neutron detector array. A neutron is detected indirectly by recoiled proton which is mainly produced by H(n,n) and ^{12}C(n,np) reaction in the plastic scintillator. The vector of neutron is determined as follows.

$$L = |\vec{r}_{\text{tgt}} - \vec{r}_n| \tag{4.36}$$

$$\beta_n = L/(\text{TOF}_{\text{NEB-tgt}} \times c) \tag{4.37}$$

$$P_n = m_n \beta_n \gamma_n \tag{4.38}$$

$$E_n = m_n \gamma_n \tag{4.39}$$

$$\vec{P_n} = \frac{\vec{r_n} - \vec{r_{tgt}}}{L} P_n \tag{4.40}$$

where, $\vec{r}_{\text{tgt}}$ is the position of the target $\vec{r}_{\text{tgt}}$, m_n is the neutron mass. In following section, the analysis of neutron events will be described.

4.4.1 Selection of Real Neutron Events

For the selection of neutron events, the events caused by charged particle and gamma ray should be rejected. In addition, in two neutron selection procedure, noise signals caused by multiple interaction of a single neutron, called cross-talk have to be eliminated. The selection of neutron events is performed in five steps as follows.

1. All events detected by the first VETO are considered to be charged particles and are rejected.

2. Among the events detected by NEBULA, events with a light output Q of less than 6 MeVee are considered to be gamma rays and are rejected.

3. Events whose TOF from the target to the first wall is less than 40 ns and whose TOF from the target to the second wall is less than 42 ns are considered to be non-neutron events with $\beta < 0.9$ and are rejected.

4. (For the selection of two neutron events) For events detected at the second VETO, detections in which the two fastest neutron events incident on the second NEUT wall are dr(xy) $<$ 500mm and 1ns $<$ dt $<$ 5ns are considered to be cluster scattering events from second VETO and the second event is rejected.

Reaction	$^{16}\mathrm{B} \rightarrow {}^{15}\mathrm{B} + n$
Beam energy	Reconstructed from ^{17}B beam profile
Relative energy	0 - 10 MeV (Uniformly generated)
Position distribution	Reconstructed from ^{17}B beam profile
Angular distribution	Reconstructed from ^{17}B beam profile

Table 4.6: The Geant4 simulation condition for cross-talk rejection

5. (For the selection of two neutron events) Cross-talk events are rejected.

After these rejection procedure, we choose the first and second fastest event as a neutron event. In following section, the three step of cross-talk rejection procedure will be described.

4.4.2 Cross-talk Rejection

The conditions of the cross-talk rejection are determined based on a Geant4 simulation. To reject the cross-talk events, $^{16}\mathrm{B} \rightarrow {}^{15}\mathrm{B} + n$ simulation is performed, thereby replicating cases where all two-neutron events are due to cross-talk. The beam ^{16}B is reconstructed based on the ^{17}B beam information at target (Figure 4.4). The details of the simulation are shown in Table 4.6.

Clustering event

The clustering event means the two events which are detected in very close distance in very small time interval. It means the second event is likely to be a recoil proton from the first event. The clustering event is rejected by the following condition.

$$\left(\frac{dr - dr_0}{3\sigma_{dr}}\right)^2 + \left(\frac{dt - dt_0}{3\sigma_{dt}}\right)^2 < 1 \tag{4.41}$$

where dr and dt are the position and time difference between two events. And dr_0 and dt_0, σ_{dr} and σ_{dt} mean the central values and the standard deviations of the distribution of dr and dt for the clustering events. The dr_0 and dt_0 are 98.35 mm and 0.65 ns, and σ_{dr} and σ_{dt} are 71.07 mm and 0.40 ns.

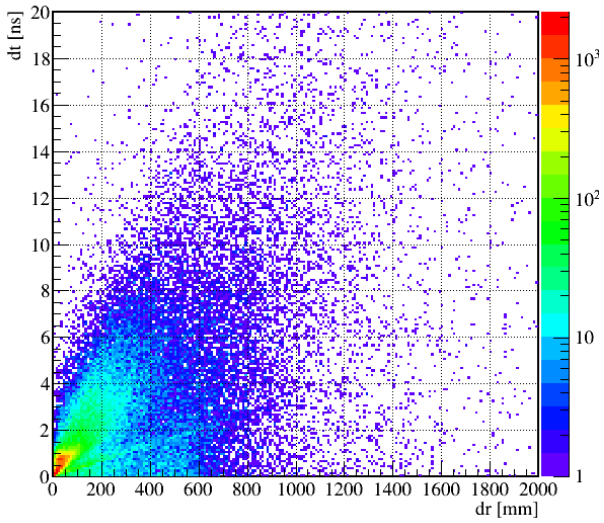

Figure 4.9: Cross-talk simulation result of clustering event

same wall event

Figure4.10 shows the cross-talk simulation result of same wall event. The right figure shows the distribution of light output of second event Q_2 with the function of relative velocity β_{01}/β_{12} and the left one shows the distribution of Q_2 with $1/\beta_{12}$. After the selection of two neutron events, each event is tagged by the hit order. The light output is tagged as Q_1 and the one of second event is tagged as Q_2. The relative velocity between two events is defined as β_{01}/β_{12} where β_{01} represents the velocity between first hit and the target and β_{12} represents the velocity between first and second hit. The cross-talk rejection condition of same wall event is defined as follows.

$$\frac{\beta_{01}}{\beta_{12}} > 1 \qquad \text{or} \qquad \frac{\beta_{01}}{\beta_{12}} < -1.5 \tag{4.42}$$

If the $\beta_{01}/\beta_{12} > 1$, it means the second event is slower than the first event and it is considered to be a cross-talk event caused by the scattered neutron from the first event. If the $\beta_{01}/\beta_{12} < 0$, it means the z position of the second event is smaller than the first event. In this case, the cross-talk event can happen by the back scattering of the neutron from the first event. The condition of $\beta_{01}/\beta_{12} <$ -1.5 is enough to reject this cross-talk event. Another cross-talk rejection condition is determined by the γ ray rejection. Considering that the γ ray events distribute in the region of

$1/\beta_{12} \sim \pm 1$, the γ ray rejection condition is defined as follows.

$$\left| \frac{1}{|\beta_{12}|} - 1 \right| < 3\sigma_\gamma \tag{4.43}$$

The events in this region with the light output of second event Q_2 less than 20 MeVee are considered to be γ ray events. The σ_γ is the standard deviation of the distribution of $1/|\beta_{12}|$ for the γ ray events. The σ_γ is 0.1.

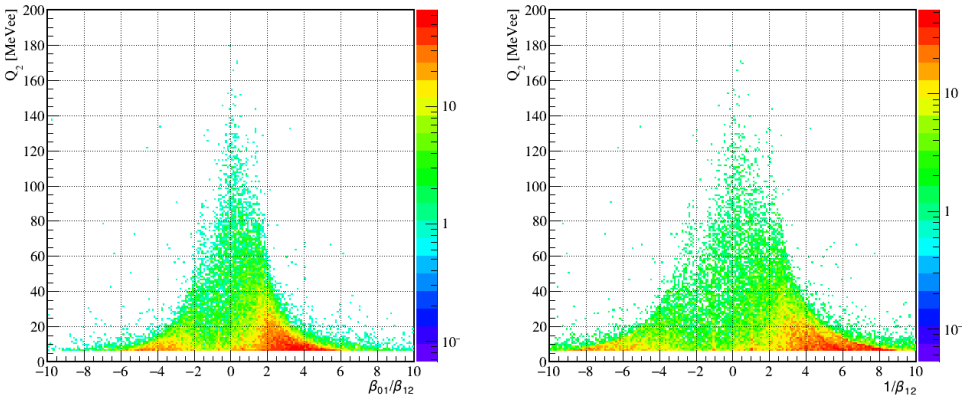

Figure 4.10: Cross-talk simulation result of same wall event

different wall event

Figure 4.11 shows the cross-talk simulation result of different wall event. The right figure shows the distribution of light output of second event Q_1 with the function of relative velocity β_{01}/β_{12} and the left one shows the distribution of Q_2 with $1/\beta_{12}$. The cross-talk rejection condition of different wall event is similar to the same wall event, but in this case, Q_1 is used for the cross-talk rejection with the relative velocity. The cross-talk rejection condition of different wall event is defined as follows.

$$\frac{\beta_{01}}{\beta_{12}} > 1 \qquad \text{or} \qquad \frac{\beta_{01}}{\beta_{12}} < -1.5 \tag{4.44}$$

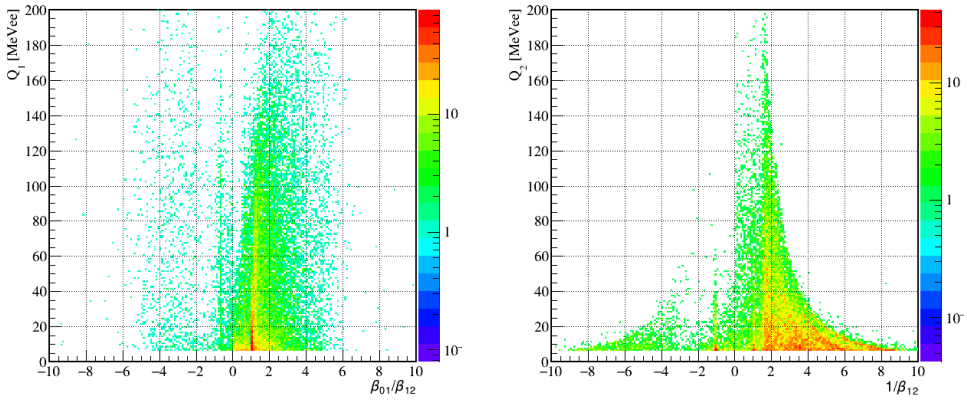

Figure 4.11: Cross-talk simulation result for different wall event

And the γ ray rejection is also performed using the distribution of Q_2 with $1/\beta_{12}$. The rejection condition is also defined as follows.

$$\left| \frac{1}{|\beta_{12}|} - 1 \right| < 3\sigma_\gamma \tag{4.45}$$

The σ_γ for different wall is 0.1.

4.4.3 Cross-talk Residual Rate

Even though we performed the cross talk rejection, there probably be residual of cross talk. For each cross talk step, we evaluated the residual rate of cross talk. Each step is as follows.

- (a) no rejection
- (b) clustering rejection
- (c) clustering rejection + same wall rejection
- (d) clustering rejection + same wall rejection + gamma rejection

The residual rate of cross talk is given by the following equation.

$$R = \frac{N_{M>2}}{N_{M>1}} \tag{4.46}$$

The multiplicity $M > 1$ event is 225385, $M > 2$ event of each step and residual rate R are written in Table 4.7. The residual rates of same and different wall cross-talk are 2.4% and 0.9% respectively, when the all cross-talk rejection conditions are performed.

Condition	same wall event (R)	different wall event (R)	all wall event (R)
(a)	89721 (39.8%)	10123 (4.5%)	99844 (44.3%)
(b)	29032 (12.9%)	16848 (7.5%)	45880 (20.4%)
(c)	6274 (2.8)%)	2791 (1.2%)	9065 (4.0%)
(d)	5352 (2.4%)	2089 (0.9%)	7441 (3.3%)

Table 4.7: The cross talk residual rate evaluation

4.5 Acceptance and Efficiency Correction

For evaluating the two-neutron detection efficiency and acceptance, the simulation is performed by Geant4. The information of simulation is as follows. The recoil effect at the reaction point is not considered in the simulation. The simulation condition is in the Table 4.8.

Physics Model	Phase Space Decay
Reaction	$^{17}\mathrm{B} \rightarrow {}^{15}\mathrm{B} + 2n$
Beam Energy	Reconstructed from ^{17}B beam profile
Relative Energy	1-10 MeV (Uniformly generated)
Scattering Angle	0-30 mrad (Uniformly generated)

Table 4.8: The Geant4 simulation condition for two-neutron detection efficiency and acceptance

The results of acceptance simulation for same and different wall are shown in figure 4.12. x axis is relative energy E_{rel} between ^{15}B and two neutrons, y axis is scattering angle θ_{scat} in laboratory coordinate and z axis is the detection efficiency. The acceptance of same wall in small E_{rel} less than 0.5 MeV is very small because of the clustering cross-talk cut. The result of two-neutron detection efficiency curve for relative energy E_{rel} is shown in figure 4.13. The blue line shows the same wall efficiency and the red line shows the different wall efficiency. The black line is the sum of the same and different wall efficiency.

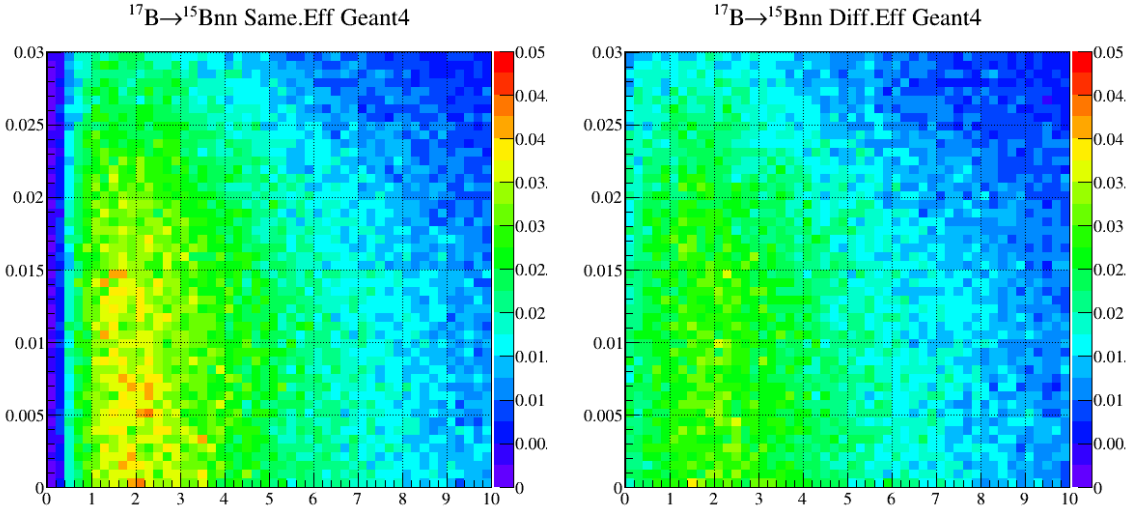

Figure 4.12: $2n$ Acceptance for same wall (left) and different wall (right)

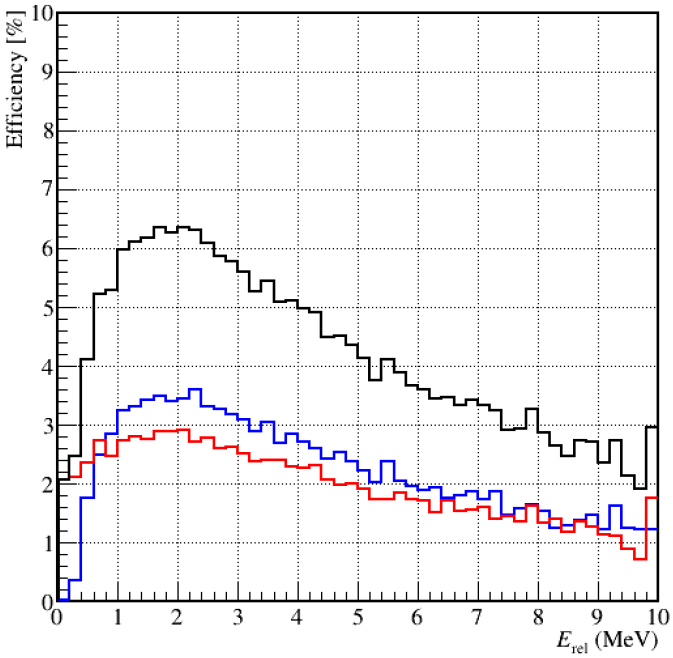

Figure 4.13: $2n$ Efficiency for same wall (left) and different wall (right)

4.6 Relative Energy Spectrum

The relative energy E_{rel} spectrum are reconstructed for the events where ^{15}B and neutron(s) are detected. Figure 4.14 shows the relative energy spectrum of ^{15}B and two neutrons. The relative energy spectrum of ^{15}B and one neutron is shown in Figure 4.15. In the figures, the blue lines are the relative energy from the Pb or C target runs and the red lines are the one from empty target which is normalized with the number of events. The empty target runs will be subtracted as a background component. The differential cross section is calculated from the relative energy spectrum as follows.

$$\frac{d\sigma}{dE_{rel}} = \frac{1}{N_t} \cdot \frac{N_i}{N_{beam}} \cdot \frac{\mathrm{LT(DSB)}}{\mathrm{LT(B \cap N)}} \frac{1}{\epsilon_{\mathrm{FDC1}} \epsilon_{\mathrm{FDC2}} \epsilon_{acc} \epsilon_{eff}}, \tag{4.47}$$

where N_t is the number of target nucleons, N_i is the number of events in the i-th bin, N_{beam} is the number of beam particles, LT(DSB) and LT(B $\cap$ N) are the live time of DSB and B $\cap$ N trigger respectively, ϵ_{FDC1} and ϵ_{FDC2} are the efficiency of FDC1 and FDC2, ϵ_{acc} is the acceptance and ϵ_{eff} is the efficiency of two-neutron detection. The differential cross section of ^{15}B and two neutrons and ^{15}B and one neutron are shown in Figure 4.16 and 4.17.

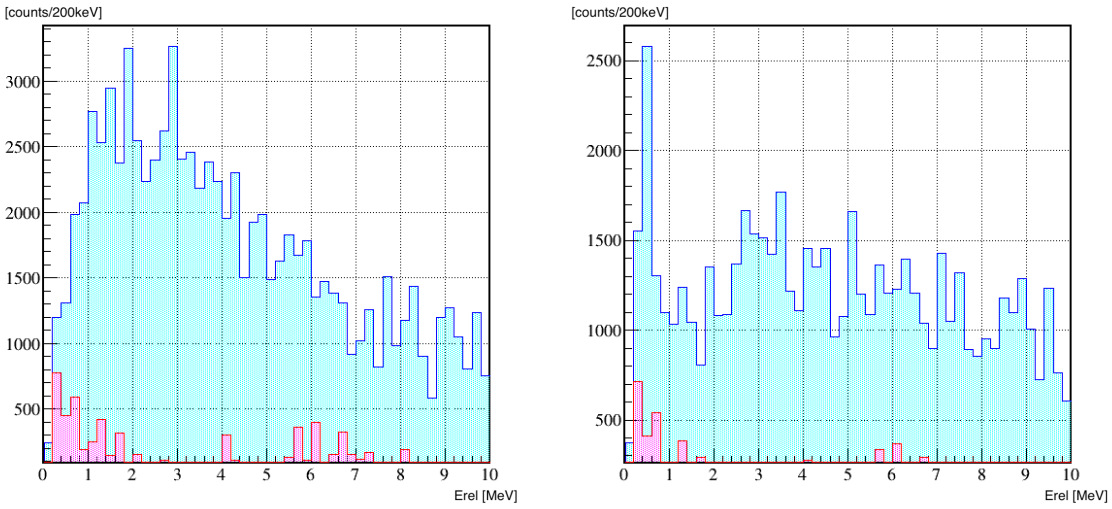

Figure 4.14: Relative Energy Spectrum of $^{15}\mathrm{B} + n + n$ at Pb target (left) and C target (right)

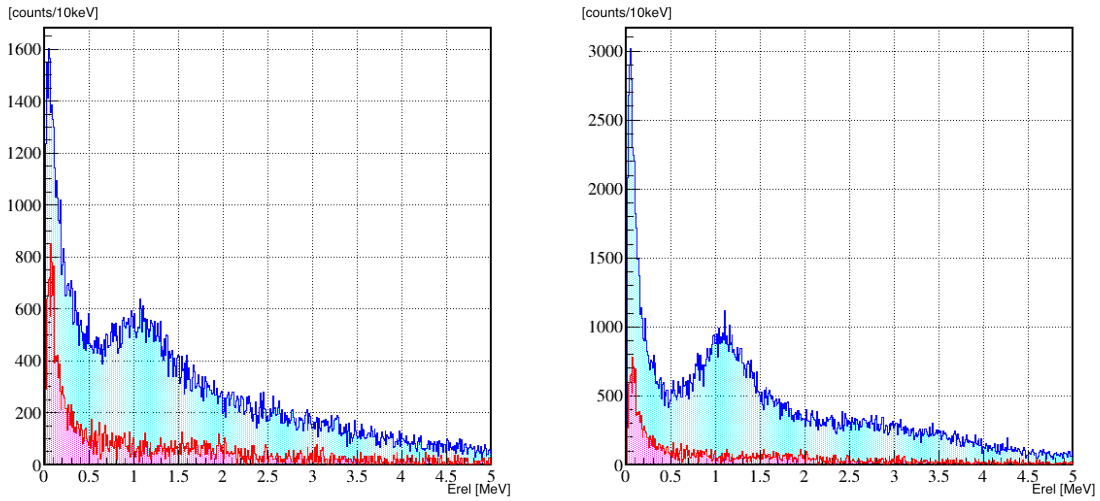

Figure 4.15: Relative Energy Spectrum of $^{15}\mathrm{B} + n$ at Pb target (left) and C target (right)

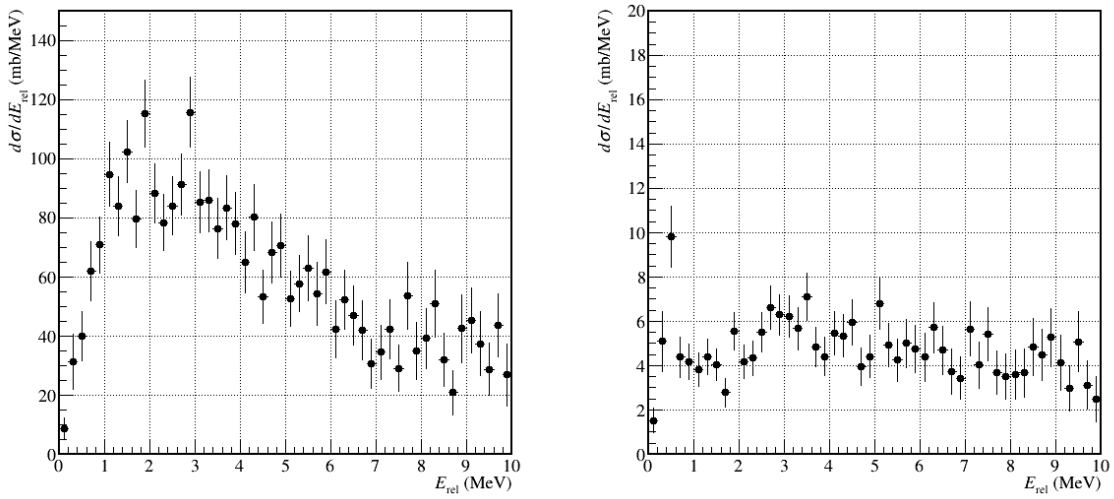

Figure 4.16: Differential cross section of $^{15}\mathrm{B} + n + n$ for Pb target (left) and C target (right)

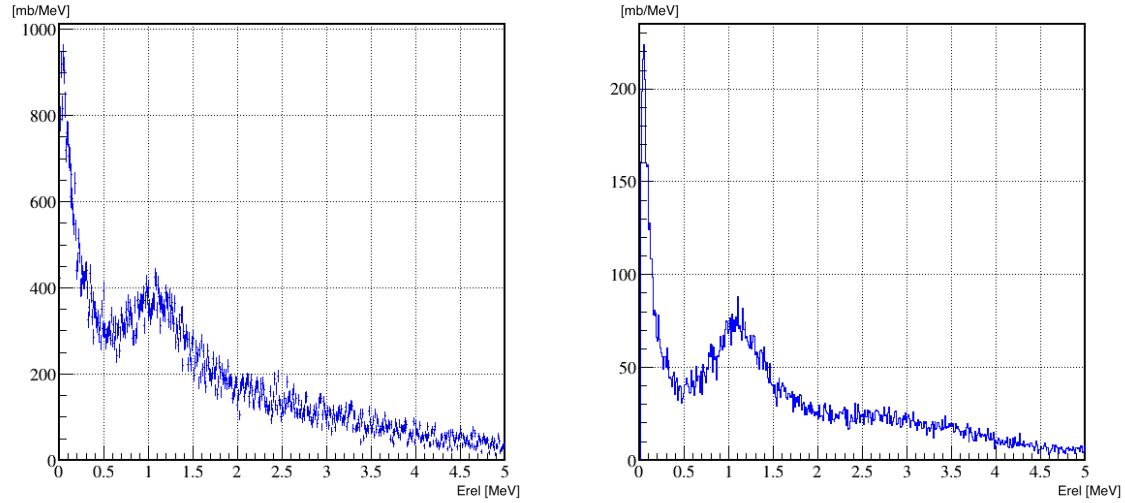

Figure 4.17: Differential cross section of $^{15}\mathrm{B} + n$ at Pb target (left) and C target (right)

Chapter 5

Result and Discussion

In this chapter, we discuss about the results obtained from data analysis. First, we discuss about the inclusive cross section of ^{17}B. In this analysis, we extracted the inclusive 2n removal cross section and 4n removal cross section. After that, we discuss about the relative energy spectra for ^{16}B +n and ^{15}B + n + n at Pb and C target. Finally, the result of Coulomb dissociation and B(E1) spectrum are discussed. Dineutron correlation is also discussed in this chapter.

5.1 Inclusive Cross Section

The inclusive cross section of ^{17}B of xn removal reaction is obtained by following formula [39].

$$\sigma_{-xn} = \frac{\sigma_R - \sigma'_R}{e^{-\sigma'_R N_t} - e^{-\sigma_R N_t}} \left(\frac{N'_{in}}{N_{in}} - \frac{N'_{out}}{N_{out}} \right), \tag{5.1}$$

where σ_R and σ'_R is total reaction cross section of beam and fragment particle respectively, N_t is the number of target per unit area. N_{in} and N'_{in} are number of beam and fragment for target-in runs respectively, and N_{out} and N'_{out} are number of beam and fragment for target-out runs. In this research, we assume that $\sigma_R \approx \sigma_{R'}$, then the formula can be simplified as

$$\sigma_{-xn} = \frac{1}{N_t} \left(\frac{N'_{in}}{N_{in}} - \frac{N'_{out}}{N_{out}} \right). \tag{5.2}$$

The calculation results of $2n$ and $4n$ removal cross section for each C and Pb target are shown in Table 5.1. The ratio between Pb and C target is also shown in the table. The ratio of 2n removal

cross section between Pb and C target was 3.9 and the ratio of 4n removal cross section was 2.4. This result is significantly smaller than the one of ^{19}B, which is 7.1. This result shows that there is less Coulomb dissociation enhancement in ^{17}B than ^{19}B.

	σ_{-2n} (mb)	σ_{-4n} (mb)
^{17}B + Pb	617(21)	154(11)
^{17}B + C	159(3)	63(2)
σ_{Pb}/σ_C	3.9	2.5

Table 5.1: Inclusive cross section of ^{17}B on Pb and C target

5.2 Coulomb Dissociation Cross Section

Coulomb dissociation cross section can be extracted by eq.(2.9) from the inelastic reaction cross section for Pb and C target. In this research, we used $\Gamma = 2.835$[27].

	$Erel < 10$ MeV	$Erel < 7$ MeV
σ_{inel}(Pb)	519(13) mb	479(11) mb
σ_{inel}(C)	47(1) mb	35(1) mb
σ_{CD}	458(14) mb	381(11) mb

Table 5.2: Coulomb dissociation cross section of ^{17}B

In Figure 5.1 shows the differential cross section distribution for ^{15}B $+n+n$ on Pb and C target. The blue dot is Pb target, and red dot is C target. The C target event is scaled by $\Gamma = 2.835$ Factor. Figure 5.2 shows the Coulomb dissociation cross section. The Coulomb dissociation cross section is 458(14) mb for $E_{rel} < 10$ MeV and 381(11) mb for $E_{rel} < 7$ MeV. It has a high and broad peak at around 2$\sim$3 MeV.

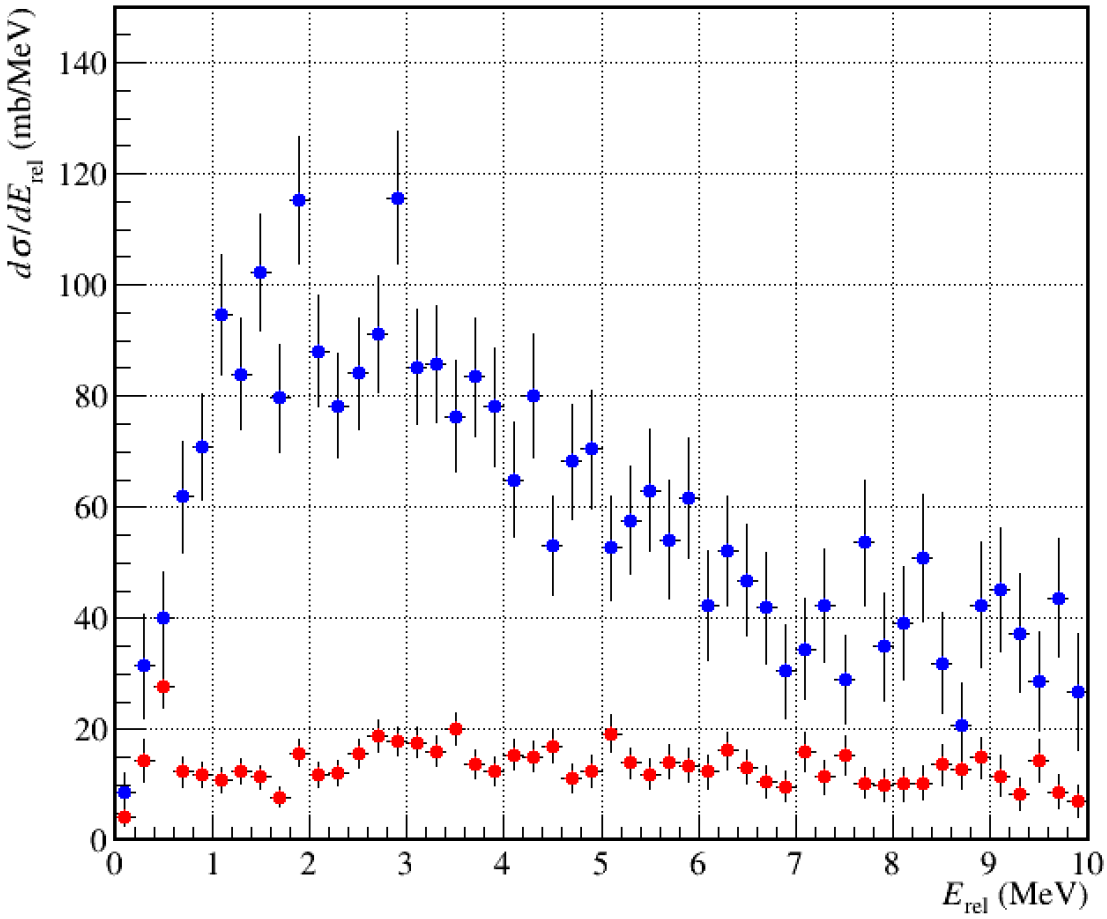

Figure 5.1: The differential cross section for ^{15}B + n + n on Pb and C target. The blue dot is Pb target, and red dot is C target. The C target event is multiplied by $\Gamma = 2.835$ factor.

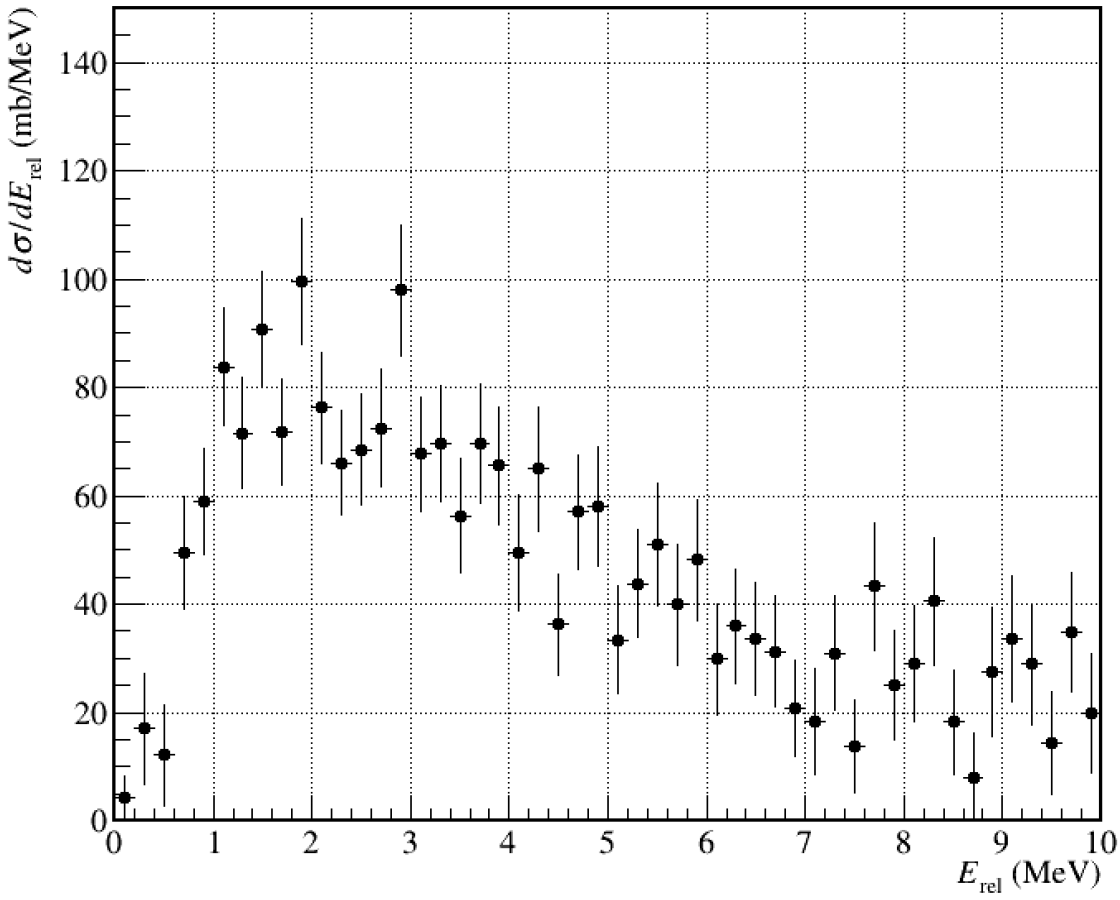

Figure 5.2: Coulomb dissociation cross section of ^{17}B

5.3 Reduced E1 Transition Probability

About reduced dipole transition probability, we can extract $B(E1)$ strength as follows.

$$\frac{d\sigma_{coul}}{dE_x} = \frac{16\pi^3}{9\hbar c} N_{\mathrm{E1}}(E_x) \frac{dB(\mathrm{E1})}{dE_x} \tag{5.3}$$

The virtual photon number is calculated by using the eq.(2.5).

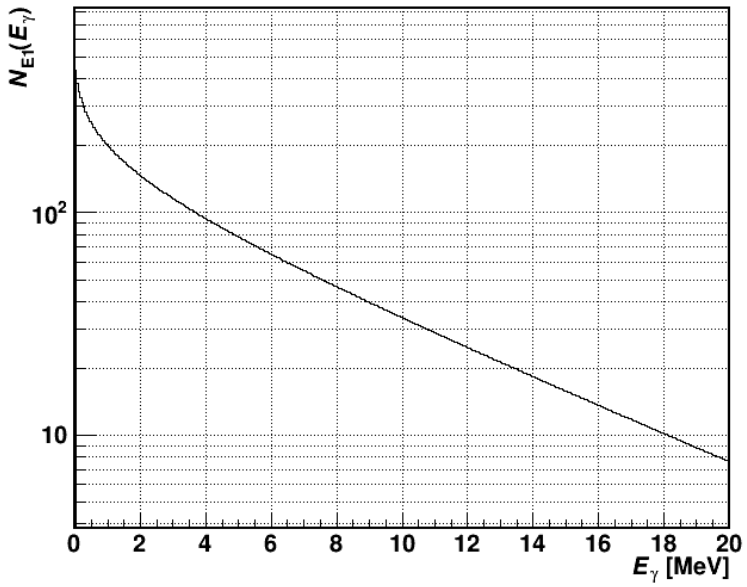

Figure 5.3: Virtual Photon Number of ^{17}B with 270 MeV/u at Pb Target

The reduced E1 transition probability B(E1) distribution is shown in Figure 5.4

$$B(E1) = \int_0^{+\inf} \frac{dB(E1)}{dE_x} dE_x \tag{5.4}$$

$$\simeq \int_0^{+10} \frac{dB(E1)}{dE_x} dE_x = 2.00 \pm 0.10 [e^2 fm^2] \tag{5.5}$$

$$\simeq \int_0^{+7} \frac{dB(E1)}{dE_x} dE_x = 1.32 \pm 0.06 [e^2 fm^2] \tag{5.6}$$

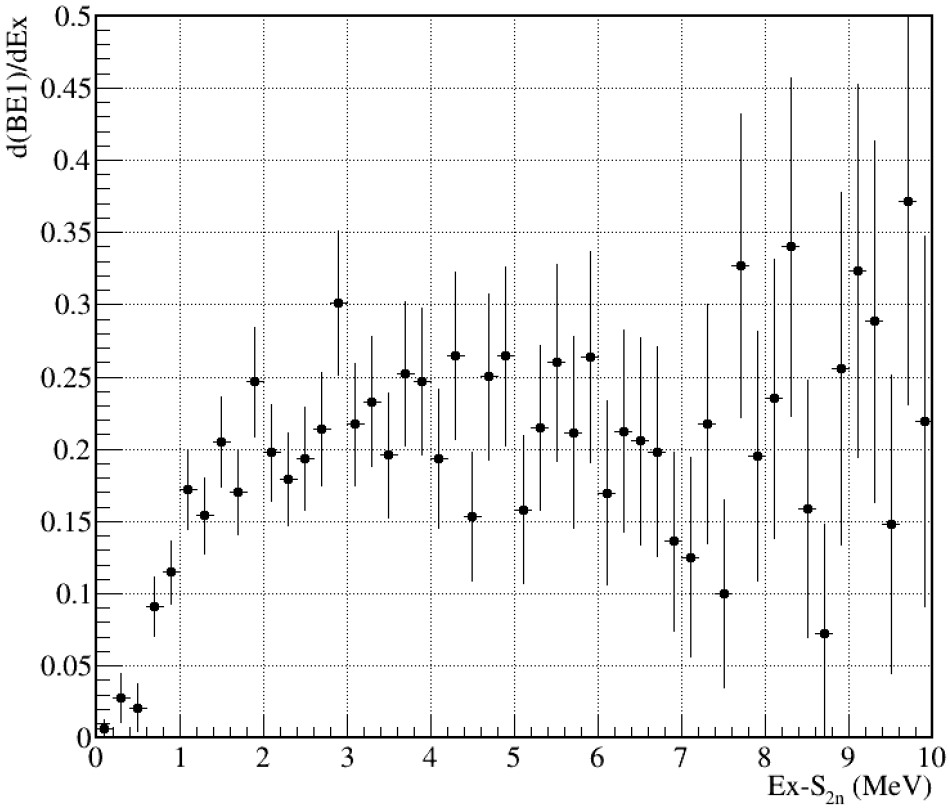

Figure 5.4: B(E1) strength of ^{17}B

5.4 Dineutron Correlation

Dineutron correlation can be calculated from $B(E1)_{tot}$ as follows.

$$B(E1)_{tot} = \frac{3}{\pi}\left(\frac{Ze}{A}\right)^2 \langle r^2_{c-nn}\rangle \tag{5.7}$$

With the obtained $B(E1)$ strength up to 10 MeV and 7 MeV, we can extract $\sqrt{\langle r^2_{c-nn}\rangle}$ respectively as follows.

$$\sqrt{\langle r^2_{c-nn}\rangle} = 4.11 \pm 0.02(stat.)\ \text{fm} \qquad (0 < E_{rel} < 10MeV) \tag{5.8}$$

$$\sqrt{\langle r^2_{c-nn}\rangle} = 3.34 \pm 0.02(stat.)\ \text{fm} \qquad (0 < E_{rel} < 7MeV) \tag{5.9}$$

Furthermore, we can extract the distance of $2n$ from three body model.

$$\langle r^2_{halo}\rangle = \frac{A_c}{A}\langle r^2_{core}\rangle + \frac{2A_c}{A^2}\langle r^2_{c-nn}\rangle - \frac{1}{2A}\langle r^2_{nn}\rangle \tag{5.10}$$

where A and A_c is the mass number of halo nucleus and core. $\langle r^2_h\rangle$ and $\langle r^2_c\rangle$ are the mean-square matter radius of halo nuclei and the core, which is 3.00(6) fm and 2.75(6) fm respectively.

$$\sqrt{\langle r^2_{nn}\rangle} = 4.48 \pm 1.78(stat.) \text{ fm} \qquad (0 < E_{rel} < 10MeV) \tag{5.11}$$

$$\sqrt{\langle r^2_{nn}\rangle} = 6.34 \pm 1.78(stat.) \text{ fm} \qquad (0 < E_{rel} < 7MeV) \tag{5.12}$$

Finally, the mean opening angle of dineutron can be extracted as follows.

$$\langle \theta_{nn}\rangle = 56.6 \pm 19.4(stat.) \text{ deg.} \qquad (0 < E_{rel} < 10MeV) \tag{5.13}$$

$$\langle \theta_{nn}\rangle = 87.0 \pm 16.6(stat.) \text{ deg.} \qquad (0 < E_{rel} < 7MeV) \tag{5.14}$$

Chapter 6

Conclusion

In this thesis, we investigated the Coulomb dissociation of two neutron halo nucleus ^{17}B with carbon and lead target at 270 MeV/u. We extracted the inclusive reaction cross section for two and four neutron removal reaction respectively. According to the $2n$ removal reaction cross section ratio between lead and carbon target, which is 3.9, the Coulomb dissociation of ^{17}B at lead target is not to be dominant as the neighboring nucleus ^{19}B which has a large $2n$ removal reaction cross section ratio, 7.1[23]. And the Coulomb dissociation cross section is also extracted from relative energy E_{rel} spectrum. The Coulomb dissociation cross section spectrum of ^{17} has a broad peak around $2 \sim 3$ MeV, which is larger than the one of other halo nuclei such as ^{11}Li[10] and ^{19}B[23]. The peak position of the Coulomb dissociation cross section spectrum is related with the strength of soft $E1$ excitation of halo nuclei, and the broad peak of ^{17}B is considered to be caused by a weak halo or a neutron skin structure. Also, by integrating the spectrum, the Coulomb dissociation cross section is obtained as 381 $\pm$ 11 mb in a range up to 7 MeV and 458 $\pm$ 14 mb up to 10 MeV. Both are significantly smaller than the one of ^{19}B which is approximately 1 b[23].

By equivalent photon method, we extracted the reduced $E1$ transition probability $B(E1)$ spectrum. The integrated $B(E1)$ value up to 7 MeV was 1.32 $\pm$ 0.06 e^{2}fm^2 and the one up to 10 MeV was 2.00 $\pm$ 0.10 e^{2}fm^2. The $B(E1)$ value for ^{19}B was 1.64 $\pm$ 0.06 (*stat*) e^{2}fm^2 in a range up to 6 MeV[23] which is larger than the one for ^{17}B. Also, compared to the shape of $B(E1)$ spectrum for ^{19}B, the $B(E1)$ spectrum for ^{17}B has very broad curve and the peak position is around $4 \sim 5$ MeV. These features indicate that the Coulomb dissociation is not dominant for ^{17}B as well as in the case of ^{19}B.

Dineutron correlation is also investigated by the opening angle of valance neutrons. The opening angle of valance neutrons in ^{17}B was 56.6 $\pm$ 19.4 degree in a range of $B(E1)$ up to 10 MeV, and

87.0 $\pm$ 16.6 degree in a range of $B(E1)$ up to 7 MeV. The average result has consistent with the recent research result, 77.4 degree by A. Corsi[40].

For the future plan, evaluation of systematical error is needed. Also the contribution of excited state of ^{17}B at the reaction point should be considered by γ ray analysis. Also the opening angle of valance neutrons and the dineutron correlation can be calculated with a three-body model can be a theoretical support.

Appendix A

Energy Loss Calculation

Energy loss calculation for beam and charged fragment particles is performed using FORTRAN code: ELOS [41]. ELOS is a computer program which calculates time propagation of a charged particle in matter. In this code, the stopping power formula extracted from RANGELBL [42] are used. The material information between F7 to target and from target to SAMURAI entrance is recalculated from reference [36] [37]

A.1 Material Between F7 to Target

Detector	Composition	Phase	Density
Vacuum	Vacuum	Gas	
Air	N_2 :78%, O_2 :21%, Ar:1%	Gas	1.205 (mg/cm^3)
Myler	$C_{10}H_8O_4$	Solid	1.400 (g/cm^3)
Kapton	$C_{22}H_{10}N_2O_5$	Solid	1.420 (g/cm^3)
Plastic	C_2H_4	Solid	1.032 (g/cm^3)
Vinylchloride	C_2H_3Cl	Solid	1.300 (g/cm^3)
Ar	Ar	Gas	1.662 (mg/cm^3)
CH_4	CH_4	Gas	0.667 (mg/cm^3)
C_4H_{10}	C_4H_{10}	Gas	2.493 (mg/cm^3)

Table A.1: Material information between F7 to target

#	Detector or Vacuum	Material Data	Thickness (cm)	Note
1	Vacuum	vacuum.dat	11.041	11.0455+0.0045=11.05
2	F7 PPAC 1	mylar.dat	0.0045	
3	F7 PPAC 2	mylar.dat	0.0045	
4	Vacuum	vacuum.dat	9.3	9.3+0.3+1.4=11.0
5	Vacuum	vacuum.dat	0.3	
6	F7 Plastic	plastic.dat	1.4	
7	Vacuum	vacuum.dat	3576.35	3576.35+69.3=3645.65
8	Vacuum	vacuum.dat	69.3	
9	Kapton	kapton.dat	0.0125	0.0125+11.9875=12.0
10	Air	air.dat	11.9875	
11	SBT1 Plastic	plastic.dat	0.05	0.05+0.02+0.0048
12	Light Shield	vinylchloride.dat	0.02	+7.9252=8.0
13	Light Shield	mylar.dat	0.0048	
14	Air	air.dat	7.9252	
15	SBT2 Plastic	plastic.dat	0.05	0.05+0.02+0.0048
16	Light Shield	vinylchloride.dat	0.02	+5.9252=6.0
17	Light Shield	mylar.dat	0.0048	
18	Air	air.dat	5.9252	
19	ICB(Window)	kapton.dat	0.003	0.003+22.98096
20	ICB(Ar)	Ar.dat	22.98096	+2.55344+0.0126
21	ICB(CH_4)	CH4.dat	2.55344	+0.0126+2.55344
22	ICB(Anode)	mylar.dat	0.0126	+22.98096+0.003=51.1
23	ICB(Cathode)	mylar.dat	0.0126	
24	ICB(CH_4)	CH4.dat	2.55344	
25	ICB(Ar)	Ar.dat	22.98096	
26	ICB(Window)	kapton.dat	0.003	
27	Air	air.dat	5.0	
28	Window	kapton.dat	0.008	0.008+14.079=14.087
29	Vacuum	vacuum.dat	14.079	

#	Detector or Vacuum	Material Data	Thickness (cm)	Note
30	BDC1(Window)	kapton.dat	0.008	0.008+8.976
31	BDC1(C_4H_{10} 100 torr)	C4H10_100torr.dat	8.976	+0.008+0.008=9.0
32	BDC1(Cathode)	kapton.dat	0.008	
33	BDC1(Window)	kapton.dat	0.008	
34	Vacuum	vacuum.dat	90.932	
35	BDC2(Window)	kapton.dat	0.008	0.008+8.976
36	BDC2(C_4H_{10} 100 torr)	C4H10_100torr.dat	8.976	+0.008+0.008=9.0
37	BDC2(Cathode)	kapton.dat	0.008	
38	BDC2(Window)	kapton.dat	0.008	
39	Vacuum	vacuum.dat	97.281	
40-1	C Target(1/2 Thickness)	carbon_1789.dat	0.5	Density: 1.789 g/cm^3
40-2	Pb Target(1/2 Thickness)	Pb.dat	0.1435	Density: 11.34 g/cm^3

Table A.2: List of material between F7 to target

#	Detector or Vacuum	Material Data	Thickness (cm)	Note
1-1	C Target(1/2 Thickness)	carbon_1789.dat	0.5	Density: 1.789 g/cm^3
1-2	Pb Target(1/2 Thickness)	Pb.dat	0.1435	Density: 11.34 g/cm^3
2	Vacuum	vacuum.dat	97.338	
3	FDC1(Window)	kapton.dat	0.016	0.016+0.012
4	FDC1(Cathode)	kapton.dat	0.012	+33.572=33.6
5	FDC1(C_4H_{10} 50 torr)	C4H10_50torr.dat	33.572	

Table A.3: List of material between target to FDC1

A.2 Energy Loss Calculation for Secondary Beam Particle

For the evaluation of the secondary beam energy at the middle of target, energy loss calculation from F7 to the middle of target have performed. The initial energy is obtained from the A/Z and the $B\rho$ at F5. After F5 to the middle of target, the energy loss calculation is performed using the ELOS code with the material information between F7 to target. The initial energy at F5 is given by the formula from [43] as,

$$E_{\mathrm{F5}} = m_u\left(\sqrt{1 + 96.52\frac{B\rho^2}{m_u(A/Z)^2}} - 1\right), \tag{A.1}$$

where m_u is the atomic mass unit, $B\rho$ is the magnetic rigidity from eq. 4.7, A/Z from eq. 4.3. The ELOSS calculation result is shown in Fig.A.1. After the ELOSS calculation, the β_{tgt} is obtained by 2nd order polynomial fitting as a function of $\mathrm{TOF}_{\mathrm{F7\text{-}F13}}$ and E_{tgt} is calculated from the β_{tgt}.

$$\beta_{\mathrm{tgt}} = p_0 \cdot \mathrm{TOF}^2_{\mathrm{F7-F13}} + p_1 \cdot \mathrm{TOF}_{\mathrm{F7-F13}} + p_2 \tag{A.2}$$

$$E_{\mathrm{tgt}} = \frac{m_u}{\sqrt{1-\beta^2_{\mathrm{tgt}}}} \tag{A.3}$$

where p_0, p_1 and p_2 are the fitting parameters.

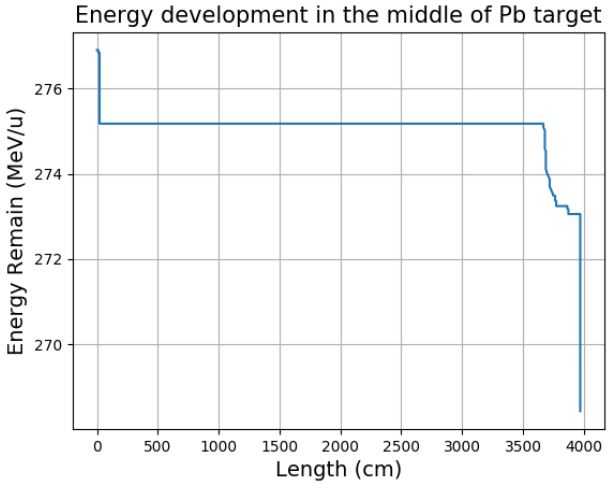

Figure A.1: Energy development for ^{17}B particle ($E_{\mathrm{F5}} = 276.9$ MeV/u) between F7 to Pb target

A.3 Momentum Push-back Calculation for Charged Fragment Particle

We obtained the momentum of charged fragment particle in the vacuum of SAMURAI magnet by Geant4 simulation. For the invariant mass calculation, the momentum in the vacuum of SAMURAI magnet should be converted to the momentum in the middle of target. The momentum push-back calculation is performed using the ELOS code with the consideration energy loss in the material between SAMURAI magnet and the middle of target. The fitting function for momentum push-back calculation is given by

$$P_{\text{SAMURAI}} = B\rho \times Z \times m_u \tag{A.4}$$

$$P_{\text{tgt}} = p_0 \cdot P_{\text{SAMURAI}} + p_1 \tag{A.5}$$

where P and $B\rho$ is the momentum and magnetic rigidity calculated by ELOSS code, Z is the charge of the particle, m_u is the atomic mass unit. P_{tgt} and P_{SAMURAI} is the momentum in the middle of target and the momentum in the vacuum of SAMURAI magnet, respectively. p_0 and p_1 are the fitting parameters. The fitting parameters are obtained by the linear fitting of the momentum push-back calculation result. Figure A.2 shows the leaner fitting result for the momentum push-back calculation of ^{15}B fragment particle for the C, Pb and empty target.

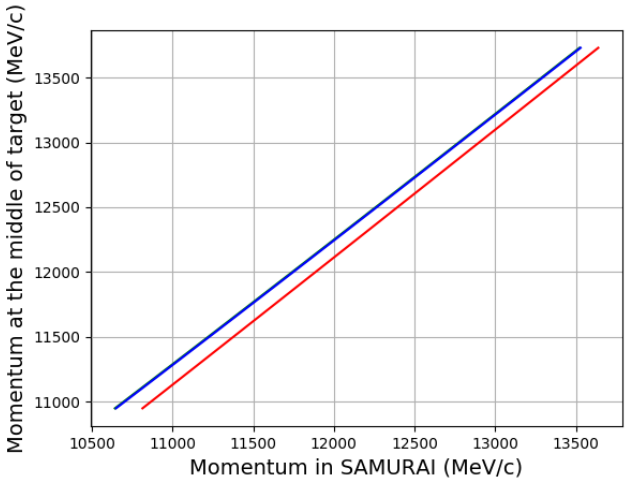

Figure A.2: Momentum push-back calculation for ^{15}B fragment particle. Blue line is for C and Pb target and red line is for empty target.

Appendix B

Intrinsic Resolution of Drift Chambers

B.1 One-dimensional Tracking

- z_i : z-position at i-th layer
- x_i : measured x-position at i-th layer
- N : number of planes
- x_0, a_0 : position and angle at the center of chamber (z = 0) determined by fitting
- Δx_i : position resolution of i-th layer
- Δx_0, Δa_0 : position and angle resolution of drift chamber

For one-dimensional tracking, a track is calculated by

$$x_0 = \frac{\sum z_i^2 \sum x_i - \sum x_i z_i \sum z_i}{N \sum z_i^2 - (\sum z_i)^2} \tag{B.1}$$

$$a_0 = \frac{N \sum x_i z_i - \sum x_i \sum z_i}{N \sum z_i^2 - (\sum z_i)^2} \tag{B.2}$$

This equations can be simplified as

$$x_0 = \frac{S_{z^2} S_x - S_{zx} S_z}{D} \tag{B.3}$$

$$a_0 = \frac{N S_{zx} - S_x S_z}{D} \tag{B.4}$$

by defining

$$S_x = \sum x_i \tag{B.5}$$

$$S_z = \sum z_i \tag{B.6}$$

$$S_{z^2} = \sum z_i^2 \tag{B.7}$$

$$S_{zx} = \sum x_i z_i \tag{B.8}$$

$$D = N \sum z_i^2 - (\sum z_i)^2 \tag{B.9}$$

B.2 Error Propagation

The position and angle resolution at the center of chamber can be calculated by error propagation of resolution of each layer Δx_i.

$$\Delta x_0^2 = \sum_{i=1}^{N} \left(\frac{\partial x_0}{\partial x_i} \right)^2 \Delta x_i^2 \tag{B.10}$$

And the resolution can be estimated to be

$$\Delta x_0 = \Delta x \sqrt{S_{z^2}/D} \tag{B.11}$$

$$\Delta a_0 = \Delta x \sqrt{N/D} \tag{B.12}$$

with the assumption that $\Delta x_i = \Delta x$ for all i.

B.3 Resolution and Residual Distribution

Residual at i-th layer is defined as

$$r_i = x_i - (x_0 + a_0 z_i) \tag{B.13}$$

$$= x_i - \frac{1}{D}(S_{z^2} S_x - S_{zx} S_z + z_i N S_{zx} - z_i S_z S_x) \tag{B.14}$$

By calculating the error propagation from eq.(B.10), we can obtain the relation between resolution of one layer Δx and width of residual distribution Δr_i.

$$\Delta r_i = \Delta x \sqrt{1 - \frac{1}{D}(S_{z^2} - 2z_i S_z + N z_i^2)} \tag{B.15}$$

B.4 Resolution Evaluation from One-dimensional Tracking

B.4.1 X and Y plane of BDCs

BDC1 X [mm]	Δr_i	Δx_i	BDC1 Y [mm]	Δr_i	Δy_i
X1 (z=-14.4)	0.1573	0.2544	Y1 (z=-4.8)	0.1591	0.2573
X2 (z=-9.6)	0.2051	0.2610	Y2 (z=0)	0.2085	0.2653
X3 (z=+4.8)	0.2096	0.2667	Y3 (z=+14.4)	0.2108	0.2682
X4 (z=+9.6)	0.1608	0.2600	Y4 (z=+19.2)	0.1620	0.2620
Average		0.2605	Average		0.2632

Table B.1: Width of residue and resolution for each BDC1 plane

BDC2 X [mm]	Δr_i	Δx_i	BDC2 Y [mm]	Δr_i	Δy_i
X1 (z=-14.4)	0.1637	0.2648	Y1 (z=-4.8)	0.1720	0.2782
X2 (z=-9.6)	0.2177	0.2770	Y2 (z=0)	0.2262	0.2878
X3 (z=+4.8)	0.2259	0.2874	Y3 (z=+14.4)	0.2241	0.2852
X4 (z=+9.6)	0.1707	0.2761	Y4 (z=+19.2)	0.1709	0.2764
Average		0.2763	Average		0.2819

Table B.2: Width of residue and resolution for each BDC2 plane

	Δx_0 [mm]	Δy_0 [mm]		Δa_0 [rad]	Δb_0 [rad]
BDC1	0.1340	0.1627	BDC1	0.01316	0.01330
BDC2	0.1422	0.1743	BDC2	0.01396	0.01424

Table B.3: Position and angular resolution of BDC1 and BDC2

B.4.2 X plane of FDCs

FDC1 X [mm]	Δr_i	Δx_i	FDC2 X [mm]	Δr_i	Δx_i
X1 ($z = -65$)	0.2854	0.3872	X1 ($z = -308.66$)	0.3185	0.4222
X2 ($z = -55$)	0.3146	0.3978	X2 ($z = -291.34$)	0.3448	0.4459
X3 ($z = -5$)	0.2841	0.3115	X3 ($z = -8.66$)	0.4450	0.4875
X4 ($z = +5$)	0.2892	0.3171	X4 ($z = +8.66$)	0.2978	0.3262
X5 ($z = +55$)	0.3302	0.4176	X5 ($z = +291.34$)	0.3031	0.3920
X6 ($z = -65$)	0.3138	0.4258	X6 ($z = -308.66$)	0.2889	0.3830
Average		0.3762	Average		0.4095

Table B.4: Width of residue and resolution for X plane of FDC1 (left) and FDC2 (right)

	Δx_0 [mm]	Δa_0 [rad]
FDC1	0.1545	0.01330
FDC2	0.1671	0.00068

Table B.5: X direction position and angular resolution of FDC1 and FDC2

B.5 X-U-V plane Tracking

Tracking using U (α angle) and V ($-\alpha$ angle) plane. The least square method in this case becomes the following matrix equation:

$$\vec{x} = M^{-1}\vec{a}, \tag{B.16}$$

where the symmetric matrix M and the vector $\vec{a}$, $\vec{x}$ are defined as

$$M = \begin{pmatrix} N_x + \cos^2\alpha(N_u + N_v) & S_{z(x)} + \cos^2\alpha(S_{z(u)} + S_{z(v)}) & \sin\alpha\cos\alpha(N_u - N_v) & \sin\alpha\cos\alpha(S_{z(u)} - S_{z(v)}) \\ \cdot & S_{zz(x)} + \cos^2\alpha(S_{zz(u)} + S_{zz(v)}) & \sin\alpha\cos\alpha(S_{z(u)} - S_{z(v)}) & \sin\alpha\cos\alpha(S_{zz(u)} - S_{zz(v)}) \\ \cdot & \cdot & \sin^2\alpha(N_u + N_v) & \sin^2\alpha(S_{z(u)} + S_{z(v)}) \\ \cdot & \cdot & \cdot & \sin^2\alpha(S_{zz(u)} + S_{zz(v)}) \end{pmatrix} \tag{B.17}$$

$$\vec{a} = \begin{pmatrix} S_x + \cos\alpha(S_u + S_v) & S_{xz} + \cos\alpha(S_{uz} + S_{vz}) & \sin\alpha(S_u - S_v) & \sin\alpha(S_u z - S_v z) \end{pmatrix}^T \tag{B.18}$$

$$\vec{x} = \begin{pmatrix} x_0 & a_0 & y_0 & b_0 \end{pmatrix}^T \tag{B.19}$$

Then we can calculate the resolution as follows:

$$\Delta x_0^2 = \sum_k \left(\frac{\partial x_0}{\partial x_k}\right)^2 \Delta x_k^2 \tag{B.20}$$

$$= \Delta x^2 \sum_k \left(\frac{\partial \sum M_{1j}^{-1} a_j}{\partial x_k}\right)^2 \tag{B.21}$$

$$= \Delta x^2 \sum_{j_1,j_2} M_{1j_1}^{-1} M_{1j_2}^{-1} \sum_k \frac{\partial \sum a_{j_1}}{\partial x_k} \frac{\partial \sum a_{j_2}}{\partial x_k} \tag{B.22}$$

$$= \Delta x^2 \sum_{j_1,j_2} M_{1j_1}^{-1} M_{1j_2}^{-1} M_{j_1 j_2} \tag{B.23}$$

$$= \Delta x^2 M_{11}^{-1}, \tag{B.24}$$

$$\therefore \Delta \vec{x}_i = \Delta x^2 (M^{-1})_{ii}, \tag{B.25}$$

since,

$$\sum_k \frac{\partial \sum a_{j_1}}{\partial x_k} \frac{\partial \sum a_{j_2}}{\partial x_k} = M_{j_1 j_2}. \tag{B.26}$$

B.6 Resolution Evaluation from X-U-V plane Tracking

B.6.1 FDCs

FDC1 U [mm]	Δr_i	Δu_i	FDC1V [mm]	Δr_i	Δv_i
U1 (z=-25)	0.2572	0.3974	V1 (z=-45)	0.2920	0.4512
U2 (z=-15)	0.2781	0.3648	V2 (z=-35)	0.2951	0.3871
U3 (z=+35)	0.3171	0.4160	V3 (z=+15)	0.2973	0.3900
U4 (z=+45)	0.3163	0.4887	V4 (z=+25)	0.2772	0.4283
Average		0.4167	Average		0.4142

Table B.6: Width of residue and resolution for U and V plane of FDC1

FDC2 U [mm]	Δr_i	Δu_i	FDC2 V [mm]	Δr_i	Δv_i
U1 (z=-208.66)	0.3234	0.4711	V1 (z=-108.66)	0.3835	0.5586
U2 (z=-191.34)	0.3509	0.4825	V2 (z=-91.34)	0.4221	0.5804
U3 (z=+91.34)	0.3779	0.5197	V3 (z=+191.34)	0.3460	0.4758
U4 (z=+108.66)	0.3500	0.5098	V4 (z=+208.66)	0.3210	0.4676
Average		0.4958	Average		0.5206

Table B.7: Width of residue and resolution for U and V plane of FDC2

	Δx_0 [mm]	Δy_0 [mm]		Δa_0 [rad]	Δb_0 [rad]
FDC1	0.1239	0.2944	FDC1	0.00289	0.00948
FDC2	0.1450	0.3443	FDC2	0.00068	0.00224

Table B.8: Position and angular resolution of FDC1 and FDC2

Bibliography

[1] I. Tanihata *et at.*, Phys. Rev. Lett. **55**, 24 (1985).

[2] I. Tanihata *et at.*, Phys. Lett. B **287** (1992), pp. 307-311.

[3] I. Tanihata, J. Phys. G: Nucl. Part. Phys. **22** (1996), pp. 157-198.

[4] I. Tanihata, H. Savajols and R. Kanungo, Prog. Part. Nucl. Phys. **68** (2013) pp. 215-313.

[5] P. G. Hansen and B. Jonson, Europhys. Lett. **4**, 4 (1h87), pp. 409-414.

[6] T. Kobayashi *et at.*, Phys. Rev. Lett. **60**, 25 (1988)

[7] K. Riisager, A. S. Jensen and P. Møller, Nucl. Phys. A **548** (1992), pp. 393-413.

[8] K. Ikeda, Nucl. Phys. A **538** (1992), pp. 355c-364c.

[9] T. Nakamura, H. Sakurai and H. Watanabe, Prog. Part. Nucl. Phys. **97** (2017), pp. 53-122.

[10] T. Nakamura *et at.*, Phys. Rev. Lett. **96**, (2006), 252502.

[11] J. D. Jackson, *Classical Electrodynamics*, Wiley, New York (1975).

[12] C. A. Bertulani, G. Baur *et at.*. Phys. Rep. **163** (1988), pp. 299-408.

[13] T. Aumann and T. Nakamura, Phys. Scr. **T152** (2013), 014015.

[14] H. Esbensen and G. F. Bertsch, Nucl. Phys. A **542** (1992), pp. 310-340.

[15] K. Hagino and H. Sagawa, Phys. Rev. C **72** (2005), 044321.

[16] C. A. Burtulani and M. S. Hussein, Phys. Rev. C **76** (2007), 051602(R).

[17] A. B. Migdal *et at.*, Soviet J. Nucl. Phys. **16**, 238 (1973).

[18] K. Hagino and H. Sagawa, Phys. Rev. C **76** (2007), 047302.

[19] M. Wang *et at.*, The AME2020 (II). Chinese Physics C **45** (2021), 030003.

[20] T. Suzuki *et at.*, Nucl. Phys. A **658** (1999), pp. 313-326.

[21] T. Suzuki *et at.*, Phys. Rev. C **89** (2002), 012501.

[22] T. Yamaguchi *et at.*, Phys. Rev. C **70** (2004), 054320.

[23] K. J. Cook *et at.*, Phys. Rev. Lett. **124** (2020), 212503.

[24] Z. H. Yang *et at.*, Phys. Rev. Lett. **126** (2021), 082501.

[25] A. Estradé *et at.*, Phys. Rev. Lett. **113** (2014), 132501.

[26] T. Nakamura, *Handbook of Nuclear Physics*, I. Tanihata *et al.* (Eds.), Springer Nature, Singapore (2023).

[27] K. Ogata and J. Singh, Private Conversation.

[28] Y. Yano, Nucl. Instrum. Methods Phys. Res. B **261** (2007), pp. 1009-1013.

[29] T. Kubo, Nucl. Instrum. Methods Phys. Res. B **204** (2003), pp. 97-113.

[30] T. Kubo *et at.*, IEEE Trans. Appl. Supercond. **17**, 2 (2007).

[31] T. Kubo *et at.*, Prog. Theor. Exp. Phys. **2012** (2012), 03C003.

[32] T. Kobayashi *et at.*, Nucl. Instrum. Methods Phys. Res. B **317** (2013), pp. 294-304.

[33] S. Takeuchi *et at.*, Nucl. Instrum. Methods Phys. Res. A **763** (2014), pp. 596-603.

[34] Y. Shimizu *et at.*, Journal of Physics: Conference Series **312** (2011), 052022.

[35] Technical Information of BigRIPS. url: https://ribf.riken.jp/BigRIPSInfo/.

[36] SAMURAI Dayone wiki page. url: http://be.nucl.ap.titech.ac.jp/ smdayone/.

[37] S. Ogoshi, Master Thesis, Tokyo Institute of Technology (2013).

[38] W. R. Leo, *Techniques for Nuclear and Particle Physics Experiments*, Springer, Berlin (1994).

[39] N. Kobayashi *et at.*, Phys. Rev. C **86** (2012), 054604.

[40] A. Corsi *et at.*, Phys. Lett. B **840** (2023), 137875.

[41] Y. Satou, ELOS code, unpublished. (1998)

[42] Code RANGELBL, unpublished.

[43] J. Defour, *et at.*, Nucl. Instrum. Methods Phys. Res. A **248** (1986), pp. 267-281.

Acknowledgements

本研究を進めるにあたり、多くの方々からご指導をいただきました。指導教授の中村隆司先生には、日本の最先端の施設で行われた SAMURAI の実験データを解析する機会を与えていただき、とても貴重な経験をさせていただきました。助教の近藤洋介氏は、実験データの解析について多くの助言をいただきました。特任准教授の佐藤義輝氏は、データ解析や物理の議論について、いつも丁寧に対応いただきました。中塚徳継氏は、短い間でしたが、データ解析ツールや実験装置についていつも親切に教えていただ、大変頼りになりました。2018 年の中村研究室メンバーに感謝します。１年間、素敵な思い出をいただき、また日本に来られるきっかけになりました。齋藤敦美氏、斗米貴人氏はドクターの先輩として、どんな質問にも関わらず熱心に答えていただきました。安田昌弘氏、山田啓貴氏は HIME のテスト実験においてたくさんの知識を教えてもらいました。松本真由子氏、島田哲郎氏、三木晴瑠氏、栗原篤志氏、藤井勇紀、安田聖氏、吉留勇起氏、研究室での楽しい思い出をいただきました。2022 年の研究室メンバー、高橋康平氏、海老名直樹氏、堀川晃太氏、松井智輝氏、礒部駆氏、大澤悠真氏、高橋里緒氏、石黒宗一郎氏、池田旭輝氏、槇村泰都氏にもたくさんの思い出をいただき、日本生活の支えになりました。

저를 일본에서 연구할 수 있게 많은 지원을 해주신 한인식 교수님께 깊은 감사 드립니다. 또한 짧지만 한국에서 학부생의 신분으로 연구를 계속 할 수 있게 배려해주신 이화여자대학교 응용핵물리 실험실의 멤버들께도 감사드립니다. 특히 허장용 박사님께서는 데이터 취득 시스템과 시뮬레이션에 대하여 많은 지식을 가르쳐 주셨습니다. 김선지 박사님께서는 사무라이 데이터 분석에 있어 깊은 조언과 고민이 있을 때마다 주저 않고 들어주셔서 대학원 생활에 큰 도움이 되었습니다. 물리교육의 동기이자 핵물리 실험 분야에서 먼저 앞서나가고 있는 채연에게는 항상 연구에 있어 좋은 자세를 배울 수 있어 고마움을 표합니다. 김다히 박사님, 한세영 박사님, 임선인 박사님, 오양희 조교님 항상 연구실에서 함께 할 수 있어서 행복했습니다. 김고운 박사님과 박수연 박사님께는 대전에 방문할 때 마다 항상 긍정적인 에너지를 주신 것에 감사를 전하고 싶습니다.

마지막으로, 언제나 하고싶은 것 다 할 수 있게 아낌없이 지원해주신 부모님께 감사드립니다. 또한 항상 마음속으로 함께 해준 동생 혜찬에게 감사를 전합니다. 그리고 언제나 한국에서 저를 응원해준 친구들에게도 감사를 전합니다. Takk til lagkameraten min Jon for engelsk korreksjon og emosjonell støtte.

This project was supported by the Research Student Scholarship from Japanese Government (Monbukagakusyo:MEXT) and Advanced Research Center for Quantum Physics and Nanoscience, Tokyo Institute of Technology.